Review of Wind–Wave Coupling Models for Large-Eddy Simulation of the Marine Atmospheric Boundary Layer

GEORGIOS DESKOS,[a] JOSEPH C. Y. LEE,[a] CAROLINE DRAXL,[a,b] AND MICHAEL A. SPRAGUE[a]

[a] *National Wind Technology Center, National Renewable Energy Laboratory, Golden, Colorado*
[b] *Renewable and Sustainable Energy Institute, Boulder, Colorado*

(Manuscript received 5 January 2021, in final form 14 May 2021)

ABSTRACT: We present a review of existing wind–wave coupling models and parameterizations used for large-eddy simulation of the marine atmospheric boundary layer. The models are classified into two main categories: (i) the wave-phase-averaged, sea surface–roughness models and (ii) the wave-phase-resolved models. Both categories are discussed from their implementation, validity, and computational efficiency viewpoints, with emphasis given on their applicability in offshore wind energy problems. In addition to the various models discussed, a review of laboratory-scale and field-measurement databases is presented thereafter. The majority of the presented data have been gathered over many decades of studying air–sea interaction phenomena, with the most recent ones compiled to reflect an offshore wind energy perspective. Both provide valuable data for model validation. We also discuss the modeling knowledge gaps and computational challenges ahead.

KEYWORDS: Wind waves; Marine boundary layer; Large-eddy simulations; Atmosphere–ocean interaction; Parameterization; Renewable energy

1. Introduction

Wind–wave interaction has been a topic of continuous research for almost a century: from Jeffreys's sheltering hypothesis (Jeffreys 1925) to the most recent high-fidelity, wave-phase-resolved, and turbulence-resolving numerical simulations (Hao and Shen 2019) and large-scale field campaigns (Black et al. 2007; Edson et al. 2007). As many physical processes rely on accurately quantifying the heat, mass, and momentum exchanges that take place at the air–sea interface, wind–wave interaction dynamics have been cardinal to many scientific and engineering disciplines: from climate and weather prediction to plankton generation models (Sullivan and McWilliams 2010; Cavaleri et al. 2012). A relatively new field that is expected to also be affected by wind–wave interaction is offshore wind energy. Currently, the total installed offshore wind energy capacity of the United States amounts to 30 MW and is expected to increase drastically over the next decade, with up to 14 GW of capacity planned to be installed off the U.S. East Coast by 2030 (Musial et al. 2019). The installation and operation of offshore large-scale wind farms have raised numerous questions about the predictability of wind and wave resources in offshore environments, including our ability to predict the mean wind speed and turbulence levels that future wind turbines will experience as well as the wave field relevant to floating offshore wind turbine dynamics. To this end, wind–wave interaction lies in the epicenter of offshore wind energy. First, wind–wave interaction together with other prevalent marine boundary layer phenomena (e.g., low-level jets) can draw a completely different picture for the dynamics of atmospheric turbulence than its land-based counterpart. For instance, a recent study by Bodini et al. (2019) showed that the turbulence levels experienced by offshore wind turbines in the U.S. East Coast can be considerably lower than those found onshore. Second, the combined aerodynamic and hydrodynamic loading on floating offshore wind turbines introduces the need to also simulate both effects simultaneously for either operational (Butterfield et al. 2007) or extreme, nonoperational event scenarios (Kim et al. 2016). In any case, better models for wind–wave interaction are key to reducing uncertainty in the simulation of offshore wind energy systems and therefore further contribute to their financial viability (Veers et al. 2019).

Despite its crucial and omnipresent role in the offshore environment, wind–wave interaction has not been fully explored for the purposes of wind turbine design. As recent as 2009, the International Electrotechnical Commission (IEC) established an offshore wind turbine international standard (IEC 2009a,b), which is used for the design of both fixed-bottom and floating wind turbines (IEC-61400-3-1, IEC-61400-3-2). Within these guidelines, the designer has to specify parameters such as a reference wind speed and turbulence intensity at hub height, averaged over a period of 10 min, and refer back to IEC (2009a) (a land-based wind turbine standard) for estimating the wind speed profile. Wind–wave interaction enters the standards only in the form of a "sea surface" roughness parameter z_0, which is calculated using the well-known Charnock relation (Charnock 1955),

$$z_0 = \frac{a_{\mathrm{ch}} u_*^2}{g}, \tag{1}$$

where g is the gravitational acceleration, u_* is the friction velocity at the air–sea interface, and a_{ch} is the Charnock parameter. According to the IEC-61400-3 standard, the designer

Denotes content that is immediately available upon publication as open access.

Corresponding author: Georgios Deskos, georgios.deskos@nrel.gov

DOI: 10.1175/JAS-D-21-0003.1

is given a choice between $a_{ch} = 0.011$ for open sea and $a_{ch} = 0.034$ for near-coastal waters. Even more interesting, most high-fidelity simulations of offshore wind turbines have also ignored the role of the coupled wind–wave dynamics (Churchfield et al. 2012; Nilsson et al. 2015; Wu and Porté-Agel 2015; Deskos et al. 2020). In fact, almost all of the state-of-the-art offshore wind farm simulators are missing the capability of resolving the phase of the underlying traveling waves (Breton et al. 2017) and only a handful of studies have considered the effect of wind–wave interaction on the power and loads of offshore wind turbines (Yang et al. 2014a,b; AlSam et al. 2015; Calderer et al. 2018).

In recent years, wind–wave interaction research has enjoyed the renewed interest from both the engineering and scientific communities. This is evident by the increasing number of large-scale field campaigns (Black et al. 2007; Edson et al. 2007) and the development of novel numerical models capable of resolving and incorporating wave motions in atmospheric turbulence simulations (Yang and Shen 2011a,b; Sullivan et al. 2014). Wave-resolving simulations are relevant to turbulence-resolving atmospheric modeling via large-eddy simulation (LES) of the airflow over regular and irregular waves. It should be noted here that large-eddy simulations of the planetary boundary layer have been performed for almost five decades and are known to yield high-fidelity data for canonical cases (e.g., flow over a horizontally homogeneous flat terrain) including the daytime buoyancy-driven boundary layer (Deardorff 1972; Moeng 1984; Mason 1988; Moeng and Sullivan 1994), the neutrally stratified atmospheric boundary layer (ABL) (Mason and Thomson 1987; Andren et al. 1994; Pedersen et al. 2014), and the nocturnal stable boundary layer (Kosović and Curry 2000; Mason and Derbyshire 1990; Basu and Porté-Agel 2006). The high accuracy of LES is because of to the fact that the larger flow structures are sufficiently resolved at the computational grid scale while smaller subgrid-scale structures can be accurately modeled (Meneveau and Katz 2000). LES has also been successfully employed to study atmospheric turbulence over complex terrain (Fedorovich 1986; Smith and Skyllingstad 2005; Chow et al. 2006). More recently, however, wave-phase-resolved simulations of the marine atmospheric boundary layer (MABL) have been undertaken (Sullivan et al. 2008, 2014, 2018b; Hao et al. 2018; Hao and Shen 2019), which have enhanced our understanding of the offshore turbulence characteristics. Wave-phase-resolved simulations require the use of more sophisticated numerical algorithms often comprising two separate but loosely coupled subsolvers, one to predict the temporal/spatial evolution of the free-surface waves and another to simulate the atmospheric turbulence or alternatively a two-phase (i.e., air/water) solver with an advanced interface-tracking algorithm (Prosperetti and Tryggvason 2009). The latter approach has not been used in large-eddy simulation of the MABL and only a handful of direct-numerical simulation (DNS) studies exist to this day (Lin et al. 2008; Yang et al. 2018). However, the former approach that employs the two subsolvers loosely coupled together at the air–sea interface is considered to be a state-of-the-art model for large-eddy simulations of the MABL. Its use in marine boundary layer simulations has helped us gain insight into the complex wind–wave interaction processes and to that extent it has also challenged the validity of the widely used Monin–Obukhov similarity theory (MOST; Monin and Obukhov 1954) in wave-driven wind cases (Sullivan and McWilliams 2010; Jiang et al. 2016). We note here that MOST provides an analytical expression for the mean velocity and temperature profiles in the lower part of the ABL also known as the ''surface layer'' (see section 2) and therefore is germane to wind energy applications. Considering the importance of wind–wave interactions in predicting the ambient atmospheric turbulence as well as the impact they may have on predicting turbine loads and power output, as it was recently demonstrated by Yang et al. (2014a,b), AlSam et al. (2015), and Calderer et al. (2018), we argue that wind–wave coupling models remain a key aspect of offshore wind energy modeling and therefore need to be thoroughly studied.

In this article, we present a comprehensive review of wind–wave coupling models that can be adopted to perform large-eddy simulations of the MABL within the context of turbulence-resolving simulations at grid scales of magnitude $O(1–15\,\text{m})$ and used in offshore wind energy applications at similar or finer resolution. We shall refer to such scale-resolving simulations within domain sizes of $O(1–50\,\text{km}^3)$ as ''microscale'' simulations. This article complements many existing reviews on the fluid dynamics of wind over waves and the marine boundary layer (Belcher and Hunt 1998; Sullivan and McWilliams 2010) and textbooks and proceedings on wind–wave interaction (Csanady and Gibson 2001; Jones and Toba 2001; Hunt and Sajjadi 2003; Janssen 2004). However, in this review, we emphasize the modeling aspects by laying out all of the crucial algorithmic components. Thereby, the remainder of this review article starts with section 2, where we introduce the main geophysical processes present in the MABL together with the governing equations used within a three-dimensional, unsteady LES framework. Next, we present the wave-phase-averaged and phase-resolved modeling techniques in sections 3 and 4, respectively. These are followed in section 5 by a brief introduction of the most recent field databases collected in offshore regions of high relevance to offshore wind energy. In section 6, we summarize the physical insights gained from performing large-eddy simulations of the MABL as well as the remaining knowledge gaps and modeling limitations of the reviewed models.

2. The marine atmospheric boundary layer structure and governing equations

The MABL is a special type of the ABL that occurs over oceans or large lakes. As such, it shares many of its features with the well-studied, land-based ABL, including a similar vertical structure. On the other hand, the physical processes of the MABL are more complex as they involve additional processes at the air–sea interface that span multiple time and length scales. Nonetheless, for the sake of simplicity, we define the vertical structure of the MABL in analogy with the land-based ABL (Stull 1988; Kaimal and Finnigan 1994; Wyngaard 2010) by splitting it into two distinct regions: the ''surface'' or ''constant-flux'' layer and a free-atmosphere-topped ''mixed'' layer, as shown in Fig. 1. The former is about 1–100 m high, and

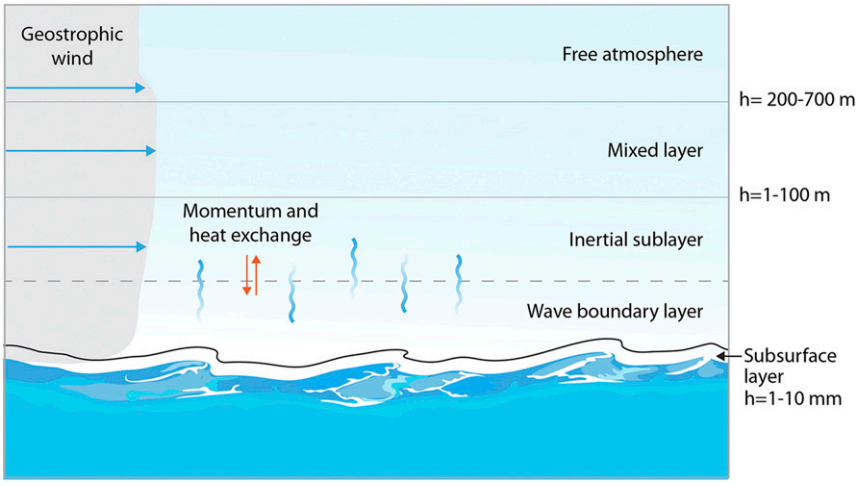

FIG. 1. Schematic representation of the atmospheric vertical structure over ocean waves.

the vertical variations of the turbulent fluxes therein are not expected to exceed 10% of their surface values. This region can be further split into the "wave boundary layer," which is the region immediately adjacent to, and directly impacted by, the motion of the waves, and the "inertial sublayer," where the bulk exchange of mass, momentum, heat, and moisture between the wind and waves takes place. The wave boundary layer is considered to be only a few meters high [$O(1\,\mathrm{m})$] for wind-driven waves and it is believed to reach higher altitudes only in cases when light winds blow over faster-moving swells (Grachev and Fairall 2001; Grachev et al. 2003). The inertial sublayer, together with the wave boundary layer, make up approximately 10%–20% of the overall boundary thickness. Above the surface layer lies the mixed layer, which, depending on the thermal stratification, can extend to altitudes of 200–700 m. Last, the free atmosphere, a stably stratified nonturbulent region above the atmospheric boundary layer, lies atop the mixed layer and its onset defines the overall MABL thickness. For completeness, we should also mention that a thin layer above the air–sea interface exists, called the surface or viscous sublayer, where viscous fluid forces are important. Thanks to the very-high-Reynolds-number nature of the MABL, $\mathrm{Re} > 10^7$, this region is only a few millimeters thick and therefore ignored in most numerical models.

The dynamics of the MABL can be described by the unsteady, compressible Navier–Stokes equations, which is common in mesoscale models [e.g., Weather Research and Forecasting (WRF) Model; Skamarock et al. 2019]. However, in microscale modeling, one can assume acoustic incompressibility to define a potential temperature θ that remains constant during isentropic displacements in the atmosphere and employ the Boussinesq approximation to account for buoyancy effects in the momentum equation. The resulting simplified model provides a framework for large-eddy simulation of the MABL, and it may take the following form:

$$\frac{\partial \tilde{u}_i}{\partial x_i} = 0, \tag{2a}$$

$$\frac{\partial \tilde{u}_i}{\partial t} + \frac{\partial}{\partial x_j}(\tilde{u}_i\tilde{u}_j) + 2\varepsilon_{ijk}\Omega_j(\tilde{u}_k - G_k) = -\frac{1}{\rho_0}\frac{\partial \tilde{p}'}{\partial x_j}\delta_{ij} - \frac{\partial \tau_{ij}^D}{\partial x_j} + \left(\frac{\tilde{\theta} - \theta_0}{\theta_0}\right)g_i, \quad \text{and} \tag{2b}$$

$$\frac{\partial \tilde{\theta}}{\partial t} + \frac{\partial}{\partial x_j}(\tilde{u}_j\tilde{\theta}) = -\frac{\partial}{\partial x_j}q_j, \tag{2c}$$

where the tilde represents a resolved-scale fluid property; u_i is the velocity field; ρ_0 is a reference density; p' is the pressure fluctuation; Ω_j is Earth's rotation vector; G_i is the geostrophic wind vector; $\tau_{ij}^D = \widetilde{u_i u_j} - \tilde{u}_i\tilde{u}_j$ is the deviatoric part of the subgrid-scale stress tensor; q_j is the subgrid-scale heat flux; θ and θ_0 are the potential temperature and its reference value, respectively; and $g_i = (0, 0, -g)$ is the gravitational acceleration vector. It is worth noting that in the LES equations of the ABL, the viscous term has been ignored because of the high-Reynolds-number nature of the flow. Subgrid-scale stress closure models have been proposed for τ_{ij}^D, from the standard Smagorinsky model (Smagorinsky 1963) to the one-equation kinetic energy model (Moeng 1984), to more sophisticated dynamic models (Meneveau and Katz 2000). The effect of the moving waves can be introduced into the previously mentioned model using two different approaches. The first is that of the wave-phase-averaged and wall-modeled LES, where a flat-bottom computational domain is used, and the wave motions are averaged in time, whereas the second and more computationally demanding approach is to resolve the wave phase and represent it in the airflow solver through a deforming "waving" boundary. The latter approach will be called the wave-phase-resolved LES model. The numerical and modeling approaches are discussed in the following sections (3 and 4).

3. Wave-phase-averaged, wall-modeled LES

In wave-phase-averaged MABL, an analogy between momentum transfers in the vicinity of a solid rough surface and that of the air–sea interface can be made. Thus, for aerodynamic

purposes, moving waves can be described through roughness elements. For both microscale and mesoscale modeling of the atmospheric boundary layer, surface fluxes are often represented by the bulk aerodynamic drag so that

$$\tau_{\text{tot}} = \rho_a C_d |U_r| U_r, \tag{3}$$

where C_d is a drag coefficient, ρ_a is the air density, and U_r is a reference velocity above the sea surface. Following the analysis of Phillips et al. (1966) and Makin and Kudryavtsev (1999), the total stress can be further decomposed into the turbulent shear stress τ_{turb}, the wave-induced shear stress τ_{wave}, and the viscous shear stress τ_{visc}, so that the sum of all three is equal to the square of the friction velocity u_*^2,

$$\tau_{\text{tot}}(z) = \tau_{\text{turb}}(z) + \tau_{\text{wave}}(z) + \tau_{\text{visc}}(z) = \rho_a u_*^2. \tag{4}$$

With these three terms supporting wind shear, the viscous shear stress is often neglected because of the high-Reynolds-number characterizing the ABL. The turbulent stress is often parameterized through the mixing-length theory, which suggests that

$$\tau_{\text{turb}}(z) = \rho_a (\kappa z)^2 \frac{du}{dz}\left|\frac{du}{dz}\right|, \tag{5}$$

where $\kappa \approx 0.41$ is the von Kármán constant and du/dz is the velocity gradient at height z. The wave-induced stress, on the other hand, may be defined through a decaying function $\mathscr{G}_d(z)$ of the wall ($z = 0$) wave-induced stress

$$\tau_{\text{wave}}(z) = \tau_{\text{wave}}(0)\mathscr{G}_d(z), \tag{6}$$

which can, in turn, be defined through a directional wave spectrum $F(k, \phi)$, for example,

$$\tau_{\text{wave}}(0) = \rho_a \int_0^\infty \int_{-\pi}^{\pi} \omega^2 F(k,\phi)\beta(k,\phi)\, dk\, d\phi, \tag{7}$$

where k and ϕ are the wavenumber and propagation angle of the waves, respectively, and $\beta(k, \phi)$ is the wave growth function. For wind-driven waves, it can be argued that $\tau_{\text{wave}}(z)$ decays very rapidly with height z, and Janssen (1989) showed that the wind profile can be defined as

$$u(z) = \frac{u_*}{\kappa} \ln\left(\frac{z + z_0 - z_b}{z_0}\right), \tag{8}$$

where z_b is the "background" roughness. Note that z_b becomes z_0 when the wave-induced stress becomes very small. This is the case in most microscale studies (Smith 1988; Fairall et al. 2003), in which the roughness length scale, is defined as the sum of the viscous-supported length scale $z_{0,s} = 0.1\nu_{\text{air}}/u_*$ and the "sea surface" roughness $z_{0,w}$ so that

$$z_0 = z_{0,s} + z_{0,w}. \tag{9}$$

This roughness scale can be used in wall-modeled LES to represent the near-surface fluid dynamics through a wall-stress model (Schumann 1975; Moeng 1984),

$$\tau_{i3}^{\text{wall}} = -C_d U_{\text{wall}} \tilde{u}_i, \quad \text{for} \quad i = 1, 2, \tag{10}$$

where $U_{\text{wall}} = \sqrt{\tilde{u}_1^2 + \tilde{u}_2^2}$ is the magnitude of the wall-parallel velocity and C_d is a drag coefficient defined as

$$C_d = \left[\frac{\kappa}{\log(z_r/z_0) - \Psi_M(z_0/L)}\right]^2, \tag{11}$$

where z_r is a reference height above the sea surface, Ψ_M is the Monin–Obukhov momentum similarity function, and $L = -u_*^3\theta_0\kappa/(gQ_0)$ the Obukhov length scale defined through the friction velocity u_* and the heat flux Q_0 at the air–sea interface. In a similar fashion, we may define the heat flux at the air–sea interface through a surface heat flux

$$q_\theta^{\text{wall}} = C_h U_{\text{wall}}(\theta_0 - \tilde{\theta}), \tag{12}$$

where

$$C_h = \frac{u_*\kappa}{\log(z_r/z_0) - \Psi_H} \tag{13}$$

is the enthalpy coefficient and Ψ_H is the Monin–Obukhov enthalpy similarity function to correct for stability effects. To estimate z_0 (hereinafter we shall assume that $z_0 \approx z_{0,w}$ because $z_{0,s} \ll z_{0,w}$), Charnock (1955) proposed a constant α_{ch} and related the roughness length scale as

$$z_0 = \frac{\alpha_{\text{ch}}}{g} u_*^2. \tag{14}$$

The values of α_{ch} have been reported to vary from 0.0144 to 0.035 (Kitaigorodskii and Volkov 1965; Garratt 1977; Wu 1980; Geernaert et al. 1986) with these differences being attributed to a number of factors such as the wind speed (Fairall et al. 2003; Edson et al. 2013), the sea state (e.g., wave age) (Donelan 1990; Smith et al. 1992; Fairall et al. 2003; Oost et al. 2002), or the water depth (Geernaert et al. 1986, 1987; Geernaert 1990; Smith et al. 1992; DeCosmo et al. 1996; Taylor and Yelland 2001; Foreman and Emeis 2010; Jiménez and Dudhia 2018). Waves tend to be rougher over shallow waters thanks to the open ocean.

a. *Wave-age and wave-steepness dependence of the sea surface roughness*

Many studies have already tried to relate z_0 to the peak (or characteristic) wave age c_p/u_*, where c_p is the peak wave-phase speed (Masuda and Kusaba 1987; Donelan 1990; Toba et al. 1990; Smith et al. 1992; Drennan et al. 2005), and all have proposed a relationship that takes the form

$$z_0^* = A_1 (u_*/c_p)^{B_1}, \tag{15}$$

where $z_0^* = z_0 u_*^2/g$ is a friction-velocity-scaled roughness and A_1 and B_1 are the two experimentally determined model parameters. These parameters have been found to vary significantly from dataset to dataset and there is no universally accepted set of values (for more details see Table 1). This is related to the fact that in Eq. (15) both the wave roughness z_0 and the wave-phase velocity are scaled by the friction velocity u_*, as was noticed by Smith et al. (1992) and Lange et al. (2004). As a remedy to this problem, Drennan et al. (2003)

TABLE 1. Table of models for the sea surface roughness length scale.

Model	$z_0^* \equiv (gz_0/u_*^2)$	z_0/H_s
Charnock (1955)	α_{ch}	$1.1\alpha_{ch}(u_*/c_p)^{3/2}$
Masuda and Kusaba (1987)	$0.0129(u_*/c_p)^{1.10}$	$0.0142(u_*/c_p)^{2.60}$
Donelan (1990)	$0.42(u_*/c_p)^{1.03}$	$0.46(u_*/c_p)^{2.53}$
Toba et al. (1990)	$0.02(u_*/c_p)^{0.5}$	$0.022(u_*/c_p)$
Smith et al. (1992)	$0.48(u_*/c_p)$	$0.53(u_*/c_p)^{5/2}$

grouped data by u_* so that any variability in wave age would arise from the waves peak phase velocity, and they proposed the following relation,

$$\frac{z_0}{H_s} = 3.35\left(\frac{u_*}{c_p}\right)^{3.4}, \tag{16}$$

where H_s is the characteristic wave height. An alternative scaling to that of the inverse wave age u_*/c_p was also proposed by Taylor and Yelland (2001), who based it on wave steepness H_s/λ_p using the peak wavelength scale λ_p. It takes the form

$$\frac{z_0}{H_s} = A_2\left(\frac{H_s}{\lambda_p}\right)^{B_2}. \tag{17}$$

The same authors found that the parameter values $A_2 = 1200$ and $B_2 = 3.4$ fit many existing datasets so that this new formulation does not exhibit a spurious correlation between z_0 and u_*. However, it was also found that their model performs poorly for very short fetches (young waves with $c_p/u_* < 15$). Alternative formulations of the wave-steepness scaling exist and often utilize the root-mean-square of the surface elevation, instead (Donelan 1990). A number of the above-mentioned models are presented in Table 1 using both the original Charnock (1955) or the significant wave height, scaling for normalizing the sea surface roughness. In addition, we plot in Fig. 2 all of the models presented in Table 1 using both scalings, as well as existing field data from the literature. We note here that the nondimensional sea surface roughness is plotted against $\omega_p^* \equiv \omega_p u_*/g$, the nondimensional angular peak frequency. This is obtained from the inverse wave age (u_*/c_p) using the linear dispersion relationship of deep-water waves $\omega_p^2 = kg$.

b. *Wave-spectra-informed sea surface*

A more systematic way to compute sea surface roughness was presented by Kitaigorodskii (1968), who used the wavenumber spectrum $F(k)$ to obtain

$$z_0^2 = A^2\int_0^\infty F(k)\exp\left[-2\kappa\frac{c(k)}{u_*}\right]dk, \tag{18}$$

where $c(k)$ is the wave-phase speed of wavelets with a wavenumber, k, and A is a model constant/parameter. The significance of Kitaigorodskii's model is that the integration of the roughness components (wavelets) are filtered by their wave age through the exponential term $\exp[-2\kappa c(k)c(k)/u_*]$, also known as the Kitaigorodskii filter. Hence, during wave growth and the shift of the wave spectral peak to lower wavenumbers the contribution to the overall roughness length is transferred to the spectral tail. Thus, to obtain the roughness length scale z_0 from Eq. (18), an empirical wave-spectrum model needs to be used. This may include a unidirectional-wave spectrum or directional-wave variance spectrum, $F(\mathbf{k})$, where $\mathbf{k} = (k_x, k_y)$ is the wavenumber spectrum. Such a spectrum is that of the Joint North Sea Wave Project (JONSWAP), which in its one-dimensional form in wavenumber space is given by

$$F_J(k) = \frac{a_J}{2k^3}\exp\left[-\frac{5}{4}\left(\frac{k_p}{k}\right)^2\right]\gamma^r, \tag{19}$$

where k_p is the wavenumber of the spectrum peak, and a_J, γ, and r are parameters of the sea state. The final wave spectrum formulation takes into account the directionality of the waves by multiplying the one-dimensional spectrum with a spreading function $D(k, \phi)$,

$$S(k,\phi) = D(k,\phi)F_j(k), \tag{20}$$

where ϕ is the wave-propagation angle. Kitaigorodskii (1973) replaced the integrated form with

$$z_0^* = 0.068(u_*/c_p)^{-3/2}\exp(-\kappa c_p/u_*), \tag{21}$$

which, however, is not consistent with the integration of Eq. (18). Other variances of the integral form can be sought through directly integrating the wave spectra, and examples can be found in the studies of Donelan et al. (1985), Banner (1990), and Elfouhaily et al. (1997).

4. Wave-phase-resolved LES

The sea surface–roughness approach provides a static representation of the wind–wave interaction and can be interpreted as a wave-informed drag model that only accounts for a downward momentum transfer (from wind to waves). However, recent studies have shown that this is not the case under swell-dominated seas where long waves propagate into light or moderate winds and where momentum can also be transferred upward (Grachev and Fairall 2001; Sullivan et al. 2008). In such a scenario, a dynamic coupling between the airflow and the propagating waves is needed. Such approaches have been pursued for airflow over monochromatic or broadband waves in either the context of direct-numerical simulations (Sullivan et al. 2000; Sullivan and McWilliams 2002; Shen et al. 2003; Kihara et al. 2007; Yang and Shen 2009, 2010; Druzhinin et al. 2012; Åkervik and Vartdal 2019; Wang et al. 2020), wall-resolved large-eddy simulations (Zhang et al. 2019; Cao et al. 2020), or wall-modeled LES (Sullivan et al. 2008; Yang et al. 2013a; Sullivan et al. 2014; Hara and Sullivan 2015; Sullivan et al. 2018a,b; Hao et al. 2018; Hao and Shen 2019). The latter approach is appropriate for the dynamic coupling between wind and ocean waves in the context of the MABL and requires the use of two separate models: a wall-model-equipped LES solver to resolve the atmospheric turbulent flow and a potential-flow solver to advance the free-surface.

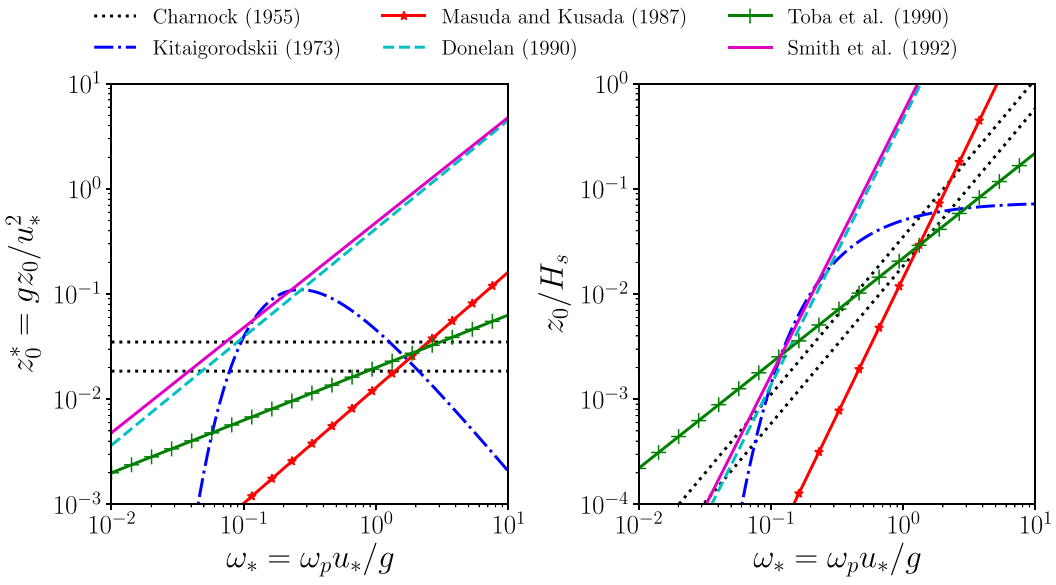

FIG. 2. Compilation of models for sea surface roughness as a function of the nondimensional angular peak frequency.

The dynamic coupling between the two models is achieved by an exchange of information at the air–sea interface. In particular, the potential-flow wave model provides information about the free-surface vertical displacement $\eta(x, y, t)$ and local orbital velocity (u_o, v_o, w_o), which in turn enters the LES solver through a waving boundary condition. The updated sea surface elevation distorts the LES mesh by moving the mesh nodes vertically to remap the computational domain. On the other hand, the LES model passes the surface atmospheric pressure fluctuations, $p'_{\text{atm}} = p_{\text{atm}} - \overline{p_{\text{atm}}}$, to the potential-flow wave solver, which is used as a dynamic boundary condition on the free surface. This approach is often referred to as "two-way coupling." In the following sections we present, for both models, their governing equations as well as modeling approaches and the coupling procedure necessary to yield the final wind–wave interaction model.

a. Potential-flow theory and wave models

To describe the evolution and propagation of water waves in the open ocean, it is often desirable to assume that the flow be incompressible, inviscid, and irrotational, which admits potential-flow theory. To this end, we may describe the wave velocity field $\mathbf{U} = \nabla\Phi$ through a potential velocity field $\Phi(x, y, z, t)$ so that

$$\nabla^2\Phi = 0. \tag{22}$$

Equation (22) is derived directly by applying a conservation of mass and assuming potential flow. Furthermore, if we assume that the wave free surface is a material surface, we may obtain the dynamic and kinematic free-surface boundary conditions, respectively:

$$\frac{\partial\Phi}{\partial t} = -gh - \frac{1}{2}|\Phi|^2 - \frac{p'_{\text{atm}}}{\rho_w} \quad \text{at} \quad z = h(x, y, t) \quad \text{and} \tag{23a}$$

$$\frac{\partial h}{\partial t} = -\frac{\partial\Phi}{\partial z} - \nabla\Phi\cdot\nabla h \quad \text{at} \quad z = h(x, y, t). \tag{23b}$$

Here, $h(x, y, t)$ represents the free-surface amplitude measured from a reference height, $z = 0$, ρ_w is the water density, and p'_{atm} is the atmospheric pressure fluctuations at the free surface. Solutions to Eq. (22) under the general form of the boundary conditions (23a) and (23b) cannot be obtained analytically because of the nonlinear nature of the dynamic free-surface boundary condition (DFSBC). Simpler solutions, however, are possible (Airy 1845; Stokes 1847; Fenton 1985) by linearization of the DFSBC and are often available in water-waves mechanics or marine hydrodynamics textbooks (e.g., Newman 1977; Dean and Dalrymple 1991). Alternative solutions include the use of numerical algorithms such as the finite-element method (Ma and Yan 2006), the boundary-element method (Longuet-Higgins and Cokelet 1976), or the high-order spectral (HOS) method (Dommermuth and Yue 1987). The latter, although it is restricted to periodic boundary conditions, is often the preferred wave model for wave-phase-resolved MABL simulations thanks to its higher accuracy and efficiency. HOS algorithms utilize the Zakharov equations (Zakharov 1968) to describe the deep-water nonlinear free-surface boundary conditions:

$$\frac{\partial h}{\partial t} = (1 + |\nabla_\perp h|^2)W - \nabla_\perp\Phi_s^2\cdot\nabla_\perp h \quad \text{and} \tag{24a}$$

$$\frac{\partial\Phi_s}{\partial t} = -gh - \frac{1}{2}|\Phi_s|^2 + \frac{1}{2}(1 + |\nabla_\perp h|^2)W^2 - \frac{p'_{\text{atm}}}{\rho_w}, \tag{24b}$$

where $\nabla_\perp$ is the horizontal gradient operator and $\Phi_s = \Phi[x, y, h(x, y, t), t]$ and $W = (\partial\Phi/\partial z)(x\ y,\ h,\ t)$ are the free-surface velocity potential and vertical velocity, respectively. Additionally, in HOS models the vertical potential gradient needs to vanish at a water depth $z = -d$,

$$\frac{\partial \Phi}{\partial z}(x, y, z = -d, t) = 0, \tag{25}$$

while periodicity is considered for the velocity potential Φ, W, and h along the two lateral directions:

$$[h, \Phi_s, W](x = 0, y, t) = [h, \Phi_s, W](x = L_x, y, t) \quad \text{and} \tag{26a}$$

$$[h, \Phi_s, W](x, y = 0, t) = [h, \Phi_s, W](x, y = L_y, t). \tag{26b}$$

The numerical implementation of the HOS method as well as further details on the wave field initialization and generation can be found in the appendix sections a and b, respectively. An example of a solution obtained via the open-source code HOS-ocean for the purpose of this review is shown in Fig. 3.

b. Computational fluid dynamics solvers using mesh motion

The need to resolve the flow within the MABL introduces the need for a waving boundary condition, i.e., an otherwise solid boundary is moving either in a prescribed fashion or in response to the airflow pressure field. Such a condition requires the numerical solvers to be able to handle mesh motion through either finite-volume/element frameworks that are based on arbitrary Lagrangian–Eulerian methods (Noh 1963; Donéa et al. 1982) or through grid-coordinate transformations (Anderson 1995, chapter 5). The latter approach has been the preferred option in the wind–wave interaction literature and a number of different algorithms have been developed (Yang and Shen 2011a,b; Sullivan et al. 2014) as a straightforward extension of existing pseudospectral or finite-difference-based computational fluid dynamics (CFD) solvers. Here, we present the governing equations, coordinate transformation, and overall implementation by adopting the notation and numerical algorithms from Sullivan et al. (2014). A similar problem formulation can be found in the work of Yang and Shen (2011a,b). Nonetheless, to obtain a wave-following system of equations we need to apply a coordinate transformation between the ''physical-space'' coordinate system (x, y, z, t) and the computational space coordinate system (ξ, η, ζ, t) $[x_i = (x, y, z, t) \Leftrightarrow \xi_i = (\xi, \eta, \zeta, t)]$ in which

$$x = \xi, \quad y = \eta, \quad z = \zeta + h(x, y, t)\left(1 - \frac{\zeta}{L_z}\right)^{\upsilon} \quad \text{and}$$

$$\frac{\partial \xi}{\partial x} = 1, \quad \frac{\partial \zeta}{\partial x} = -\frac{\partial z}{\partial \xi}, \quad \frac{\partial \zeta}{\partial z} = J, \quad \text{and} \quad \frac{\partial z}{\partial t} = -\frac{\partial \zeta}{\partial t}\frac{1}{J},$$

where $h(x, y, t)$ is the time-varying surface wave height, and here $\upsilon = 3$ is the mesh dampening coefficient (Fig. 4).

With these definitions, we may rewrite the LES Eqs. (2a), (2b), and (2c) as

$$\frac{\partial U_i}{\partial \xi_i} = 0, \tag{27a}$$

$$\frac{\partial}{\partial t}\left(\frac{\tilde{u}_i}{J}\right) + \frac{\partial}{\partial \xi_j}[(U_j - \delta_{3j} z_t)\tilde{u}_i] = \frac{F_i}{J}, \quad \text{and} \tag{27b}$$

$$\frac{\partial}{\partial t}\left(\frac{\tilde{\theta}}{J}\right) + \frac{\partial}{\partial \xi_j}[(U_j - \delta_{3j} z_t)\tilde{\theta}] = \frac{Q_i}{J}, \tag{27c}$$

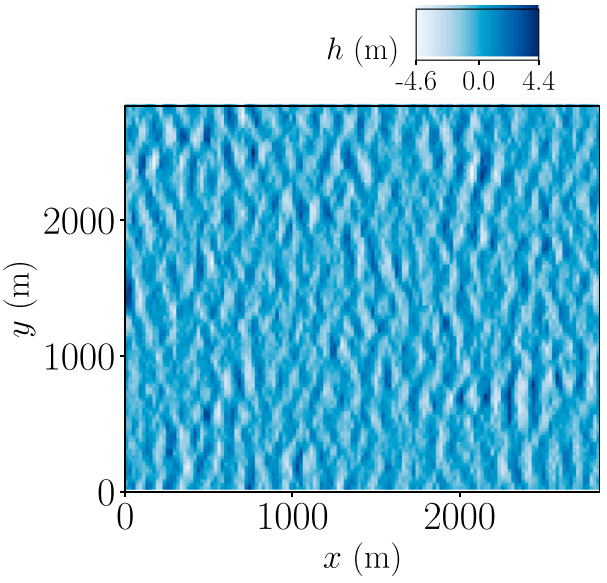

FIG. 3. Example of an irregular wave field produced by an HOS model. The presented results correspond to irregular JONSWAP waves, with a peak period $T_p = 10$ s, assuming that the atmospheric pressure fluctuations forcing term is zero ($p'_{\text{atm}}/\rho_a = 0$). The computational domain has dimensions of $20\lambda_p \times 20\lambda_p$ and is discretized using 256×256 nodes. The presented snapshot was originally generated for the purposes of this review using the open-source code HOS-ocean (Ducrozet et al. 2016).

where F_i and Q_i are right-hand-side momentum and heat terms defined via

$$\frac{F_i}{J} = -\frac{\partial}{\partial \xi_j}\left(\frac{\tilde{p}'}{J}\frac{\partial \xi_j}{\partial x_i}\right) - \frac{\partial}{\partial \xi_j}\left(\frac{\tau_{ij}^D}{J}\frac{\partial \xi_j}{\partial x_i}\right) + \left(\frac{\tilde{\theta} - \theta_0}{J\theta_0}\right)g_i + 2\varepsilon_{ijk}\Omega_j\frac{(\tilde{u}_k - G_k)}{J}g \quad \text{and} \tag{28a}$$

$$\frac{Q_i}{J} = -\frac{\partial}{\partial \xi_j}\left(\frac{\tau_{i\theta}}{J}\frac{\partial \xi_j}{\partial x_i}\right). \tag{28b}$$

Here, both the momentum and potential-temperature advection terms are written in the strong flux-conservation form using the contravariant flux velocity $U_i = (U, V, W)$,

$$U_i = \frac{u_j}{J}\frac{\partial \xi_i}{\partial x_j}. \tag{29}$$

The incompressibility condition is guaranteed by also solving for the pressure Poisson equation,

$$\frac{\partial}{\partial \xi_i}\left(\frac{1}{J}\frac{\partial \xi_i}{\partial x_j}\frac{\partial \xi_m}{\partial x_j}\frac{\partial p^*}{\partial \xi_m}\right) = S, \tag{30}$$

where S is a force proportional to the divergence field of the advection term.

1) GEOMETRIC CONSERVATION LAW

Another important aspect of the ''wave following'' solver is the satisfaction of the so-called geometric conservation law

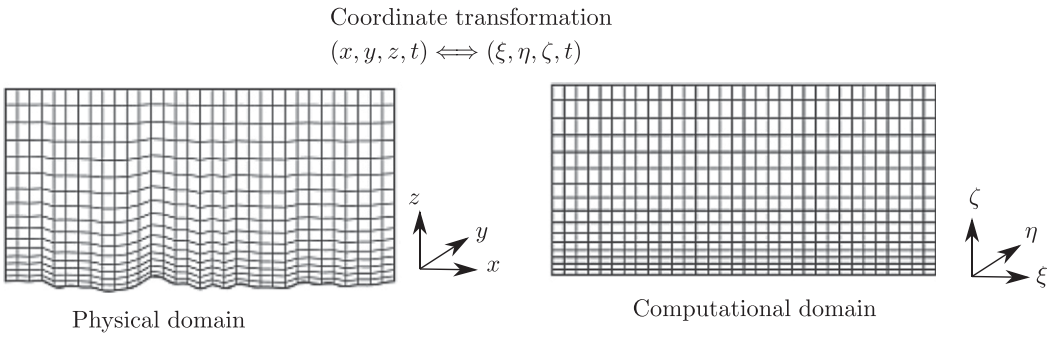

FIG. 4. Schematic representation of the coordinate transformation between the physical and computational domains. The figure is adopted from Yang et al. (2013a).

(GCL), which should guarantee that the discrete system of equations under mesh motion conserves its volume (Thomas and Lombard 1979; Demirdžić and Perić 1990). Thus, in a coordinate transformation formulation, the GCL needs to satisfy the following condition:

$$\frac{\partial}{\partial t}\left(\frac{1}{J}\right) + \frac{\partial}{\partial \xi_i}\left(\frac{1}{J}\frac{\partial \xi_i}{\partial t}\right) = 0. \tag{31}$$

Furthermore, using the previously described coordinates transformation, the GCL further simplifies to

$$\frac{\partial}{\partial t}\left(\frac{1}{J}\right) - \frac{\partial}{\partial \zeta}\left(\frac{\partial z}{\partial t}\right) = 0. \tag{32}$$

General-purpose CFD algorithms that do not utilize the "coordinate transformation" approach will need to follow a more generic formulation (e.g., Mavriplis and Yang 2006).

2) Boundary conditions and surface fluxes

While the shape of the wavy surface and its movement partly define the boundary conditions through mesh motion, the velocity and wall-stress (surface flux) boundary conditions also need to be considered. It is worth emphasizing here, that although the wave-phase-resolved simulations resolve the wave-coherent structures, they also rely on wall modeling to account for the subgrid-scale wave motions. Starting with the velocity boundary condition, the total time rate of change of the wave height $h(x, y, t)$ is

$$\left.\frac{Dz}{Dt}\right|_{\text{fs}} = \frac{Dh}{Dt} = w_{\text{o}} = \frac{\partial h}{\partial t} + \frac{\partial h}{\partial x}u_{\text{o}} + \frac{\partial h}{\partial y}v_{\text{o}} \quad \text{at} \quad \zeta = 0. \tag{33}$$

If we require an impenetrable boundary condition in the wall-normal direction (ζ direction), we then need to set the contravariant velocity, $W = \partial h/\partial t$. Similarly, the top velocity boundary condition is set to $W = z_t = 0$ at $\zeta = Z_L$. Because no mesh motion takes place under the other two directions (streamwise and lateral), the two velocity boundary conditions are simply set to $U = u_{\text{o}}$ and $V = v_{\text{o}}$. Next, stresses/surface fluxes at the wall can be computed using the wall-stress models described in section 3. These surface fluxes, however, need to be computed in the local wave-fitted coordinate system assuming the law-of-the-wall formulas. Thus, at each grid node, we define the two tangential vectors, $\mathbf{t}_1$ and $\mathbf{t}_2$, a surface normal vector, $\mathbf{n} = \mathbf{t}_1 \times \mathbf{t}_2$, as well as a relative filtered velocity vector, $\tilde{\mathbf{u}}_s = \tilde{\mathbf{u}}_w - \tilde{\mathbf{u}}_a$ as the difference between the water waves velocity $\tilde{\mathbf{u}}_w$ and the airflow velocity $\tilde{\mathbf{u}}_a$ above it. To that end, the shear-stress tensor is defined as

$$\tau' = -C_d|\tilde{\mathbf{u}}_s|[\tilde{u}_s^{(1)}\mathbf{t}_1 + \tilde{u}_s^{(2)}\mathbf{t}_2], \tag{34}$$

where the prime represents a shear-stress tensor aligned with the local, transformed coordinate system and the surface heat as

$$Q^* = C_h|\tilde{\mathbf{u}}_s|(\theta_0 - \tilde{\theta}). \tag{35}$$

The bulk-transfer coefficients, C_d and C_h, are again computed using the MOST arguments of a flat surface. One parameter that needs to be entered here is z_0. Only this time z_0 does not represent the roughness coming from all wavelength scales but only of the unresolved ones. Most studies with wave-phase-resolved simulations have adopted small values—for example, $z_0 = 2 \times 10^{-4}$ in Sullivan et al. (2008)—to represent the roughness coming from the unresolved waves. However, Yang et al. (2013a,b) investigated five different dynamic sea surface roughness models, which take into account the underlying wave spectra, namely, the "root-mean-square model," the "geometry model," the "steepness-dependent Charnock model," the "wave-kinematics-dependent model," and the "combined-kinematics-steepness model." They found that the wave-kinematics-dependent model based on the idea of Kitaigorodskii and Volkov (1965), which accounts for both the wave amplitude information (through the wave spectrum function) and the kinematics of wind and wave relative motion (through an exponential function that depends on the ratio of wave-phase speed to wind-friction velocity), yields the best performance.

c. *Wave motion via the immersed boundary method*

An alternative solution to the mesh-motion wind–wave coupling can be sought by using the immersed boundary method (IBM), first introduced by Peskin (1972). Since its conception, the IBM has been used in numerous fluid mechanics problems and engineering applications (Mittal and Iaccarino 2005; Griffith and Patankar 2020) and it is in general considered a robust and mature approach to resolving the fluid

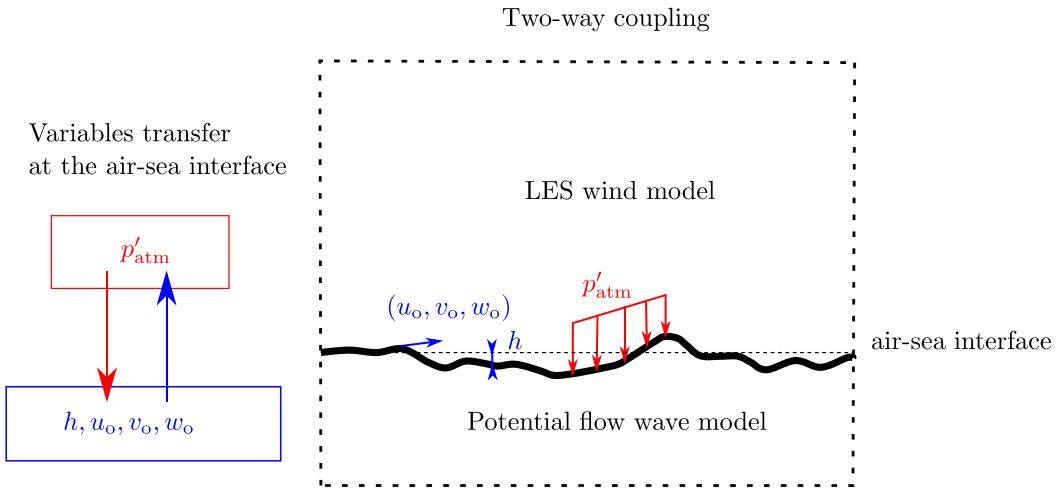

FIG. 5. Schematic representation of the two-way coupling between the LES wind model and the potential-flow wave model.

flow over complex geometries. From an implementation point of view, IBM does not require geometry-conforming meshes and the influence of a solid boundary on the fluid flow is realized through a boundary force. In incompressible solvers, the force is applied during an intermediate time step and through the Poisson equation solved within the projection method to ensure that the flow field remains divergence-free everywhere in the domain. In the context of the atmospheric boundary layer, IBM has been used to resolve the airflow over complex terrain (Bao et al. 2018; Arthur et al. 2020; Liu and Stevens 2020) and in general two variants of the method have been proposed. In the first approach, the velocity just above the terrain surface is reconstructed to fit a profile given by similarity theory (e.g., MOST) and it is referred to as the velocity-reconstruction immersed boundary method (VR-IBM) (Bao et al. 2018; DeLeon et al. 2018), whereas in the second the shear stress in the vicinity of the immersed surface is reconstructed using similarity theory, and it is therefore referred to as the shear-stress reconstruction method (SR-IBM) (Diebold et al. 2013; Ma and Liu 2017; Liu and Stevens 2020). The latter approach resembles the boundary condition of the geometry-conforming moving meshes just mentioned earlier as surface fluxes are calculated along the immersed boundary using the local tangential and normal vectors. Finally, it is worth noting that while to the best of our knowledge the IBM has not been applied to wind–wave interaction problems yet, its extension to moving boundaries can be straightforward as previous studies on moving objects and fluid–structure interaction have already proved its feasibility (Griffith and Patankar 2020).

d. Interface between the wind LES and wave HOS models

Regardless of the airflow discretization strategy (geometry-conforming moving mesh/moving immersed boundary) a coupling procedure is needed to provide a two-way (or dynamic) coupling between the wind and wave models. Thus, at each time step, the wave field is forced by the wind by incorporating the atmospheric pressure fluctuations into the dynamic boundary condition. The wave solution is integrated in time for Δt, and the wave elevation h and orbital velocity field $\mathbf{u}_o = (u_o, v_o, w_o)$ are updated. These, in turn, are used by the LES model to adapt the geometry of the domain boundary (and its mesh thereafter), as well as apply a new velocity boundary condition at each mesh node. The LES model advances in time as well, and the coupling procedure is repeated. The interface is shown schematically in Fig. 5. Note here that a number of LES studies (e.g., Yang et al. 2013a) do not consider the airflow's feedback to the wave model. This is because of the fact that the time scale for the wave to evolve under wind-driven conditions is much larger than the advection and turnover time scales of turbulent eddies and thus near-surface pressure variations (Liu et al. 2010). In that case, the magnitude of the time step needed by the two models may differ by an order of magnitude, with the LES solver often imposing a stricter Courant–Friedrichs–Lewy (CFL) number condition. For instance, in the very recent two-way-coupled study of Hao and Shen (2019) undertaken for the evolution of wind-driven (slow) waves, the time step of the coupled HOS-LES simulations was chosen to be $8.7 \times 10^{-3} \times T_p$, where T_p is the waves' peak period, whereas at the same time, the high-order spectral method of Dommermuth and Yue (1987) could have allowed for a larger time step to be used based on the local CFL number. On the other hand, in swell-dominant (fast moving) wave scenarios, the wave solver may be the one to dictate the time step size. To this end, from a numerical point of view, the two models may exchange information less or more frequently and oftentimes allow one of the solvers to advance its solution multiple time steps before exchanging information with the other one. Last, but not least, extra care should be taken to account for any differences in the spatial resolution used by the two models. In the simple case where the horizontal mesh resolution of the LES model is identical to the wave model, the mapping between the two models' mesh is straightforward. However, oftentimes the two models may employ different degrees

TABLE 2. Most recent validation datasets suited for model validation of coupled wind–wave LES.

Field campaign	Location	Duration	Selected references
FINO1	North Sea, Europe	June to November 2015 for oceanic variables; 2004 onward for atmospheric variables	Bakhoday-Paskyabi et al. (2018), Muñoz-Esparza et al. (2012), Fischer (2006)
FINO1 by-product	North Sea, Europe	—	Senet et al. (2012)
FINO1 by-product	North Sea, Europe	2011–12	Li and Lehner (2013)
FINO2	Baltic Sea, Europe	2007 onward	Hallgren et al. (2020), Sjöberg et al. (2015)
FINO3	North Sea, Europe	2009 onward	Tangvald (2012), Fischer et al. (2012)
DOE lidar buoy data	U.S. East Coast	2014 onward	U.S. Department of Energy
CBLAST low wind	Massachusetts	2001–03	Edson et al. (2007), Crescenti et al. (2001)
CBLAST Hurricane	Western Atlantic Ocean	2002–05	Chen et al. (2007), Black et al. (2007), Bell et al. (2012), Drennan et al. (2007), French et al. (2007), Zhang et al. (2008)
TOGA COARE	Western Pacific Ocean	1992–93	Webster and Lukas (1992)

of refinement, thus, an interpolation algorithm may also be needed.

5. Measurement data for model validation

Validation datasets have historically been critical to model development with field campaigns and their reported data extending over five decades: Atlantic Trade Wind Experiment (ATEX; Dunckel et al. 1974), Air Mass Transformation Experiment (AMTEX; Mitsuta 1979), Joint Air–Sea Interaction (JASIN; Pollard et al. 1983), Marine Remote Sensing (MARSEN; Geernaert et al. 1986), Canadian Atlantic Storms Program (CASP (Stewart et al. 1987), Coastal Ocean Dynamics Experiment (CODE; Zemba and Friehe 1987), Frontal Air–Sea Interaction Experiment (FASINEX; Li et al. 1989), COARE (Webster and Lukas 1992), Humidity Exchange over the Sea (HEXOS; DeCosmo et al. 1996), Surface Wave Dynamics Experiment (SWADE; Donelan et al. 1997), Risø Air–Sea Exchange (RASEX; Johnson et al. 1998), Flux, État de la mer et Télédétection en Condition de fetch variable (FETCH; Drennan et al. 2003), and CBLAST (Black et al. 2007; Edson et al. 2007). Herein, we summarize some of the most recent field studies in Table 2 that recorded comprehensive and publicly available measurement data as well as laboratory-scale experimental data that are suitable for model validation.

We start with the Tropical Ocean Global Atmosphere (TOGA) COARE, which is one of the widely used datasets for validating atmosphere–ocean coupling (Webster and Lukas 1992). The campaign took place in the equatorial western Pacific from 1992 to 1993, and advanced our understanding of climatic patterns and oscillations. In addition to conventional meteorological and oceanic measurements of the campaign (e.g., buoy), ship radars and aircraft observations were also deployed. Research using this dataset related to wind energy includes a study on near-surface wind spectra and variability across spatial and temporal scales in offshore environments (Wikle et al. 1999) and a comparison of TOGA COARE observations with reanalysis winds.

Additionally, the ongoing atmospheric and oceanic measurements at Forschungsplattformen in Nord- und Ostsee (FINO) 1, 2, and 3 platforms have been widely analyzed by researchers (Bakhoday-Paskyabi et al. 2018; Muñoz-Esparza et al. 2012; Fischer 2006; Senet et al. 2012; Li and Lehner 2013; Hallgren et al. 2020; Sjöberg et al. 2015; Tangvald 2012). Their meteorological records for over a decade in northern Europe support climatological studies on offshore wind energy applications. Muñoz-Esparza et al. (2012) used the observations to validate turbulence fluxes and atmospheric stability from planetary boundary layer schemes in mesoscale simulations. Bakhoday-Paskyabi et al. (2018) used the Reynolds stresses to quantify the distortions induced by wind turbine wakes in the marine boundary layer; whereas more recently, Patton et al. (2019) examined the role of wind–wave misalignment on the variability of nondimensional surface roughness when swells are prominent. Note here that the instrumentation differs on each platform, and in general FINO1 and FINO3 are considered to provide more detailed and accurate atmospheric and oceanic measurements.

In the United States, the CBLAST project spanned multiple years and provides valuable observed data for model validation. The two iconic branches of CBLAST were dedicated to hurricanes (Chen et al. 2007; Black et al. 2007; Bell et al. 2012; Drennan et al. 2007; French et al. 2007; Zhang et al. 2008) and low-wind conditions (Edson et al. 2007; Crescenti et al. 2001), respectively. The campaign recorded aircraft, surface-based atmospheric, and oceanic measurements along the East Coast in the summer months between 2001 and 2005. Chen et al. (2013) developed a wind–wave-coupling parameterization and used the CBLAST-Hurricane results for model validation. Sullivan et al. (2008) used CBLAST-LOW field measurements to validate wind–wave-coupled LES simulations in swells, and they emphasized the importance of wave state in simulating marine-surface drag.

In the ongoing effort to collect offshore wind measurements in the United States, the U.S. Department of Energy, New York State Energy Research and Development Authority, and Massachusetts Clean Energy Center are deploying floating lidars along the East Coast (Filippelli et al. 2015). The near-surface meteorological and oceanic measurements supplement the lidar data. The U.S. Department of Energy Office of Energy, Efficiency and Renewable Energy (EERE) announced in

April 2020 a funding opportunity (EERE 2020) for an offshore wind resource measurement and modeling science topic area to provide funding for an offshore field study to address a need to improve offshore wind resource characterization. The increasing field observations in the United States aim to reduce the uncertainty in offshore wind resource assessment. In addition to large-scale field measurements, experiments at the laboratory scale have also been used to study wind–wave interaction (Karaki and Hsu 1968; Stewart 1970; Hsu et al. 1981; Hsu and Hsu 1983; Mastenbroek et al. 1996). The latter study of Mastenbroek et al. (1996) provided evidence that validates the rapid distortion theory of turbulence above the critical layer, with important implications for turbulence closure models. More recently, Veron and coworkers performed a series of extensive laboratory measurements of the airflow above waves, using the laser-induced fluorescence and particle image velocity techniques and have provided measurements of the momentum-flux budget above waves by varying the wave age and wave steepness parameters (Buckley and Veron 2016, 2017; Buckley et al. 2020; Yousefi et al. 2020). Their detailed experimental data have also been used for validating LES studies such as that of Husain et al. (2019). Additionally, Grare et al. (2013, 2018) collected measurements at laboratory scale to estimate the momentum transfers that take place around the critical layer as well as information about the mean profiles and associated fluxes near the water surface. Finally, it is worth mentioning two additional laboratory-scale studies, the first by Donelan (2018) on the decrease of the sea drag coefficient as a result of breaking or nonbreaking flow separation during high winds, and the second by Troitskaya et al. (2012) also on the effect of surface-drag saturation but explained by a quasi-linear model of the air boundary layer above the wavy water surface.

6. Discussion

The computational approaches and experimental campaigns have shed light on wind–wave interactions. However, our understanding of these processes is far from complete. To emphasize the need to further pursue the development of wind–wave parameterizations and coupled models, it is important to briefly introduce some of the key phenomena taking place during wind–wave interactions, and existing theories that have attempted to explain the various mechanisms, as well as the impact of high-fidelity models in advancing our understanding.

a. *The role of high-fidelity modeling in advancing our understanding of wind–wave interaction*

The relationship between wind and waves can, in general, be considered a nonequilibrium one. Wind and waves are considered to be in equilibrium when the wave spectrum does not change with fetch and wind is balanced by wave dissipation (through breaking) and wave-to-wave nonlinear interactions (Csanady and Gibson 2001). To this end, wind–wave equilibrium has been the basis for the development of most sea surface roughness parameterizations as one may unambiguously define the wind–wave state via the wave age c_p/U_r, where U_r is a reference near-surface wind speed (e.g., U_{10} is the mean wind speed 10 m above the sea surface). Alternatively, the friction velocity, u_*, can be used. Thus, equilibrium is achieved when $c_p/u_* = 30$ or $c_p/U_r = 1.2$, the sea state is considered to be growing when $c_p/U_r < 1.2$ (wind-driven waves regime), and when $c_p/U_r > 1.2$ it is considered to be old (wave-driven wind regime). Starting with wind-driven waves, a number of theories have been developed over the last century starting with the sheltering hypothesis of Jeffreys (1925). The most prominent one has been the theory developed by Miles (1957) and later refined by Miles (1959a,b, 1962, 1967) that describes the generation mechanism and growth of wind waves through the so-called "critical-layer" mechanism. The "critical layer" is assumed to be a horizontal layer at a height z_c above the moving waves at which $U(z_c) = c$, where U is the mean wind speed and c is the wave-phase speed. Miles's theory recognizes the resonant interaction between water waves and the airflow, wave-induced pressure fluctuations aloft as the main mechanism and predicts exponential growth that is on the order of magnitude of the air-to-water density ratio ρ_w/ρ_a (Janssen 2004). Although Miles's theory oversimplified the problem by following a quasi-laminar approach and ignoring the turbulence effects (except when considered for the mean flow), it can still be justified for typical ocean conditions (Janssen 2004). Aspects of Miles's theory have been confirmed by turbulence-resolving simulations, such as the DNS data of Kihara et al. (2007), Shen et al. (2003), Sullivan et al. (2000), and Yang and Shen (2010), which have identified a region of closed streamlines, also known as the cat's-eye pattern, which centered about the critical-layer height, for a wide range of wave-age values, c_p/u_*. Note here that what allows the clear detection of the critical layer is also the sufficiently large wave age that can be easily reproduced by a DNS study. Other theories, such as those of Belcher and Hunt (1993) and Cohen and Belcher (1999) involve the use of the rapid distortion theory of Batchelor and Proudman (1954) and have been used to introduce the "nonsheltering" mechanism, which together with Miles's critical-layer mechanism provide a more complete explanation and leading-order estimates for the growth rate of both slow- and fast-moving waves. The wave-growth rate γ can be calculated via

$$\frac{\gamma}{\omega} = \frac{1}{\omega E}\frac{dE}{dt} = \frac{\rho_a}{\rho_w}\left(\frac{c_p}{u_*}\right)^2 \beta, \tag{36}$$

where E is the energy transferred from the wind to the waves and β is the wave-growth rate parameter. The use of turbulence-resolving simulations in both DNS and LES studies has provided good estimates for β, which is calculated numerically (Li et al. 2000) via

$$\beta = \frac{2}{\lambda (ak)^2}\int_0^{\lambda} \frac{p}{\rho_a u_*^2}\frac{\partial h}{\partial x}dx. \tag{37}$$

Sullivan and McWilliams (2002) and Yang and Shen (2010) provided estimates for β using DNS of idealized monochromatic waves and found an overall good agreement with experimental data and the analytical solution of Miles (1993). A more realistic case was considered by Hao and Shen (2019) using LES over a JONSWAP spectrum. To calculate β, Hao and Shen (2019) make use of the technique proposed by Liu et al. (2010), which requires decomposing both the pressure

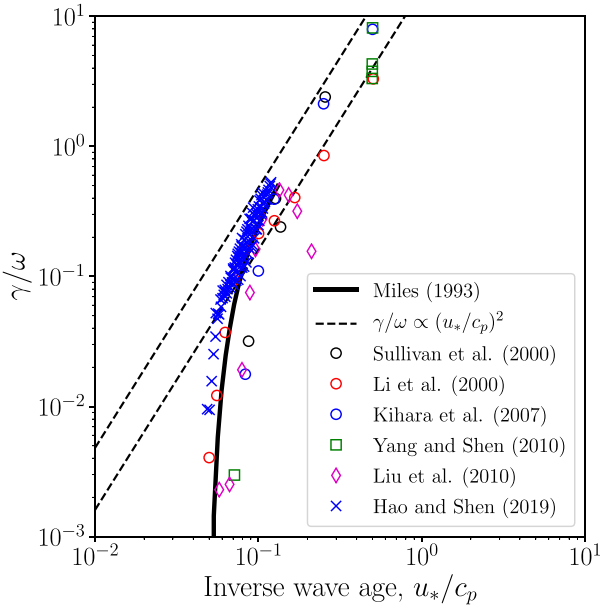

FIG. 6. Comparison of wave growth rates according to Miles's theory with high-fidelity DNS and LES numerical simulations.

and wave amplitude fields in the Fourier space. Estimates of both DNS and LES models are shown together with experimental data in Fig. 6. Moreover, the study of Hao and Shen (2019) was able to both demonstrate and quantify the existence of nonlinear interactions in the wind-forced wave field, which results in a frequency downshift with wave-phase-resolved LES simulations for the first time.

On the other side of the equilibrium line lies the case of wave-induced winds (i.e., swell-dominated seas) for which $c_p/U_r > 1.2$. Swells are long, fast-moving, and remotely generated waves, which can propagate for long distances without experiencing significant dissipation, often in direction misalignment with the local light winds. The presence of swells induces turbulent stresses that invalidate the use of the MOST. Traditionally, large-scale field campaigns have been able to show the deviation of the surface stresses from the mean wind speed (Grachev and Fairall 2001; Grachev et al. 2003; Li et al. 2018). To this end, high-fidelity LES simulations have been performed to study atmospheric turbulence above in swell-dominated seas for both neutral atmospheric stability (Sullivan et al. 2008), and a convective boundary layer (Nilsson et al. 2012). These two solutions have modeled the swell as Airy (linear and monochromatic) waves, $h = A\cos[k(x - ct)]$, where A is the wave amplitude, x is the propagation direction of the wave, and c is the wave speed calculated via the deep-water dispersion relation $c^2 = g/k = g\lambda/(2\pi)$.

A three-dimensional snapshot of simulations conducted for this article is shown in Fig. 7. The simulations correspond to wind-following waves using the open-source CFD model Nalu-Wind, which is part of the ExaWind simulation suite (Sprague et al. 2020). In the figure, contours of the velocity and vorticity fields are shown, highlighting the organization and alignment of the large-scale vertical motions with propagating waves. The role played by the upward transfer of momentum can also be calculated using wave-phase-resolved simulations and compared with existing measurements. For example, Sullivan et al. (2008) conducted quadrant analysis of the vertical momentum flux for both wave-following and wave-opposing waves and compared it with data from the CBLAST campaign (Edson et al. 2007; Smedman et al. 1999) and laboratory-scale measurements from Buckley and Veron (2016). The comparison is shown in Fig. 8 by plotting the normalized ratio of negative-to-positive-momentum-flux quadrants $-(Q_2 + Q_4)/(Q_1 + Q_3)$, where $Q_1 = (u' > 0, w' > 0)$, $Q_2 = (u' < 0, w' > 0)$, $Q_3 = (u' < 0, w' < 0)$, and $Q_4 = (u' > 0, w' < 0)$, against wave age $c_p/U_r\cos\phi$ modified by the alignment angle ϕ. Here, the values of Q_1, Q_2, Q_3, and Q_4, represent the joint probability density function of the velocity fluctuations u' and w' belonging in their respective quadrants. It is clear that $-(Q_2 + Q_4)/(Q_1 + Q_3)$ reaches its peak at the proximity of $c_p/(U_r\cos\phi) = 0$, which indicates that for a stationary rough (or wavy) wall, the transfer is downward (from the wind to the waves). On the other hand, at a sufficiently large absolute wave age a balance between negative and positive flux contributions is achieved [i.e., $-(Q_2 + Q_4)/(Q_1 + Q_3) \approx 1$], which implies that the drag force becomes nearly zero (Sullivan et al. 2008). From Fig. 8 we observe another wind–wave regime, that of the fast-propagating ($c_p/U_r > 1.2$) but wind-opposing waves ($\cos\phi < 0$). Wind-opposing simulations have been considered by only a few studies; Mastenbroek (1996), Sullivan et al. (2008), and Cao et al. (2020) have shown that the wave influence on the airflow exhibits features very different from that of the wind-following waves at the same wave age. These features include high sea-drag forces, small surface wind speed, large momentum flux, and high velocity variance. Additionally, based on detailed wall-resolved LES, Cao et al. (2020) noted that in contrast with wind-following waves, opposing waves induce "a significantly stronger vertical velocity perturbation that is out-of-phase with the wave surface ... resulting in a nearly antisymmetric spatial distribution of the wave-induced vertical velocity" in the air.

An intermediate regime describing the mixed sea states should also be discussed in context of high-fidelity simulations of the MABL. This regime may include the coexistence of a strong wind forcing and a propagating swell. Such cases have been examined, for example, in Sullivan et al. (2018b,a) using LES and direct comparisons with laboratory-scale experimental data. Some of the key findings of these simulations have explained aspects of the wave-breaking mechanism and its connection to the intermittent airflow separation, the fact that wave slope and surface drag are well correlated, as well as the premise that short waves support the bulk of the ocean wind stress, primarily thanks to the passage of a transient, strongly forced wave group that can enhance the form drag. Numerical simulations of a spectrum of waves at different wind conditions were examined by Sullivan et al. (2014). In particular, they conducted wave-phase-resolved simulations by using four different geostrophic-wind forcing values (U_G = 5, 10, 20, and 25 m s^{-1}) thus examining wave-age scenarios from swell-dominated seas (c_p/U_r = 4.2) to sea states that approach a wind–wave equilibrium (c_p/U_r = 1.1). The study showed that

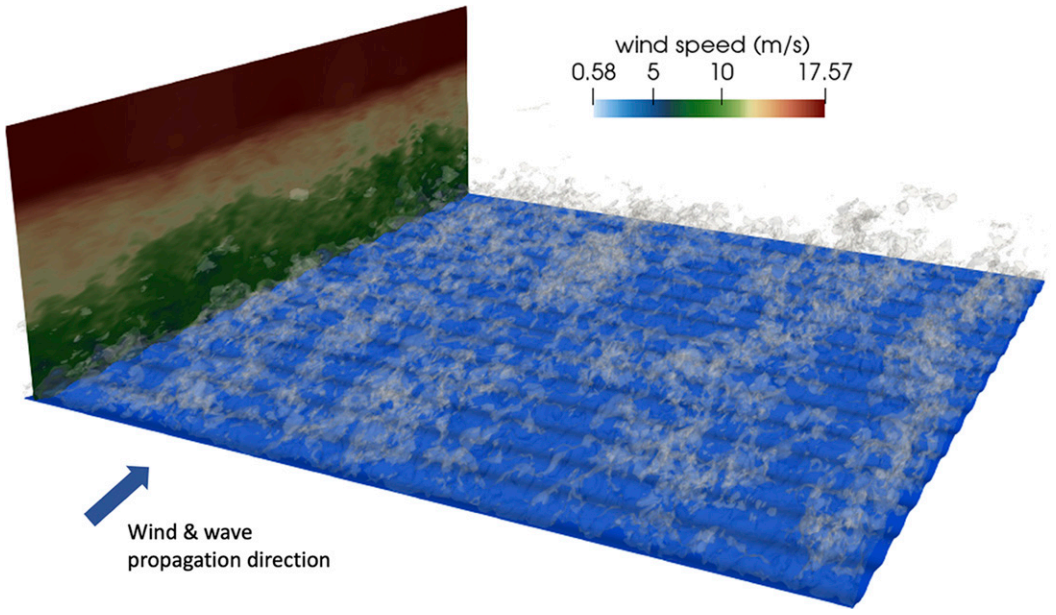

FIG. 7. Snapshot of the velocity and vorticity atmospheric fields over a swell. The numerical simulation was obtained using the open-source software framework Nalu-Wind (Sprague et al. 2020).

for low winds and a strong swell, the signature of the waves can be detected well above the reference height $z_r = 10$ m. On the other hand, as the wind–wave system approaches its equilibrium, the wave-induced turbulent motions are confined within a smaller region well below the reference height. It is also worth mentioning that for the wind–wave equilibrium cases, the LES data of Sullivan et al. (2014) were found to agree well with MOST for the lower 20% of the boundary layer (surface-flux layer) and deviate significantly for the swell-dominated cases. A similar suite of large-eddy simulations was undertaken more recently by Patton et al. (2019), using a broadband wave spectrum with swell propagating into the domain with a zero and nonzero alignment angle ($\phi = 0°$, 45°, 90°, 135°, 180°, and −90°). They found that misaligned winds/waves can increase the surface pressure drag by nearly a factor of 2 relative to the turbulent stress when a swell propagates at 180° in comparison with the pressure-gradient forcing (wind-opposing waves).

It is also important to refer to some key findings from studies that have utilized wave-phase-resolved techniques within offshore wind farm simulations. Yang et al. (2014a) conducted simulations of an infinite offshore wind farm using the Calaf et al. (2010) setup. In their study, however, instead of solely using a flat-bottom boundary and a sea surface–tuned wall-stress model, they also conducted wave-phase-resolved simulations using both a fetch-limited wave spectrum based on the JONSWAP model and a fully developed condition described by the Pierson and Moskowitz (P–M) spectrum. The comparison between the use of the two spectra showed that using fully developed spectra conditions leads to faster-moving waves and therefore exerts less resistance to the wind. To this end, the wind field in the turbine layer is relatively stronger in the P–M wave cases than in the JONSWAP cases. In the turbine-arrays simulations, wind turbines are represented by actuator disks with hub heights of 100 m and rotor diameters of 100 m. Wind-induced waves are found to have appreciable effect on wind farm performance and can increase the array-aggregate power output up to 8%. It is important to stress here that the role of modeling wave effects within wind farm simulations has been previously diminished or even ignored (e.g., Breton et al. 2017) based on the argument that wave-induced quantities decay exponentially with height. However, Yang et al. (2014a) argue that the vertical transport of momentum and kinetic energy are enhanced by the wave motion and therefore a larger vertical flux enters the turbine layer and becomes available to the turbine. In follow-up work, Yang et al. (2014b) examined

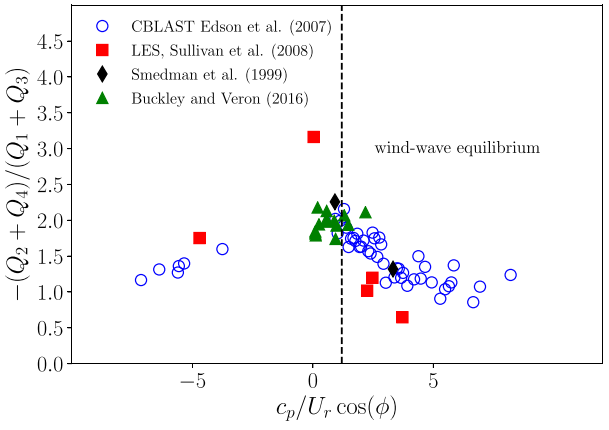

FIG. 8. Variation of the vertical-flux ratio $-(Q_2 + Q_4)/(Q_1 + Q_3)$ (defined via quadrant analysis) with wave age $c_p/(U_r \cos\phi)$. The figure is adopted from Sullivan et al. (2008).

the role of swells on the same layout. With a swell interacting with wind turbines, the mean power can be increased by a surprising 18.9% from the respective "swell absent." In addition to the mean-power effect, they found that a temporal oscillation of extracted wind power appears at the swell frequency and can be as much as 6.7% of the power output magnitude. Last, AlSam et al. (2015) examined the impact of swells on a stand-alone, fixed-bottom offshore wind turbine using the actuator line technique and the National Renewable Energy Laboratory (NREL)-5MW reference offshore wind turbine (Jonkman et al. 2009) and found that its wake can be extended to a larger downwind distance in the swell cases relative to a flat-surface-case scenario.

b. *Knowledge gaps and limitations of MABL LES*

Despite the fast development and recent interest in the microscale modeling of the marine boundary layer, a number of fundamental and practical questions remain. Starting with the wave-phase-averaged (sea surface drag) models, a number of studies have been published in recent years (e.g., Taylor and Yelland 2001; Foreman and Emeis 2010; Jiménez and Dudhia 2018). However, a number of open questions remain with regard to the representation of wave effects in cases far from wind–wave equilibrium, such as swells with wind–wave misalignment (Grachev et al. 2003; Chen et al. 2018, 2020). Existing roughness-length parameterizations have been found to perform poorly in regions of swell, and therefore more sophisticated "sea-surface roughness" length parameterizations, which take into account both the swell magnitude and direction, need to be developed. To date, the misalignment of the mean wind with the wave stress direction has been addressed only by a handful of studies (Janssen 1991; Rieder et al. 1994; Porchetta et al. 2019; Zou et al. 2019; Porchetta et al. 2021) and our understanding and modeling capabilities are far from complete. As these parameterizations were originally derived for the open ocean, certain modifications are needed for the shallower coastal waters that are more relevant to offshore wind farms (Jiménez and Dudhia 2018). To this end, a depth-dependent relationship will ultimately improve the "sea surface" roughness calculations and therefore the applicability of the wall-shear-stress models.

As far as the wave-resolved simulations are concerned, the picture drawn from recent high-fidelity simulations is encouraging. Two-way coupling models can better predict the sea surface drag coefficient and momentum fluxes as well as the wind input to the waves, such as the wave growth rate. However, LES predictions of the wave growth rate are still down by a factor of two when compared with existing analytical theories (Miles 1957, 1993). Nonetheless, a number of challenges remain for wave-phase-resolved simulations. These include the constraints and limitations imposed by the computational cost of such methods. The resolution requirements imposed upon the LES solver as a result of the resolution of short-crested waves can exceed today's high-performance-computing resources even for standard computational domains (on the order of a few kilometers) and time periods of a few-thousand wave periods T_p, $O(1000T_p)$. These limitations have been highlighted by a number of recent studies including Hao and Shen (2019). In addition, with the currently available two-way-coupling models, energy dissipation as a result of wave-breaking is excluded from any wave-phase-resolved analysis. This leads to either an unrealistic wave growth or constraining our analysis to only weak wind speeds to avoid wave-breaking. Thus, in future models, wave breaking needs to be considered through either direct modeling (e.g., two-phase fluid solvers) or accurate parameterizations. The latter approach remains an attractive and possibly easier extension of existing models; however, it may require substantial validation through comparisons with field and laboratory-scale data.

7. Concluding remarks and future direction

Our understanding of, and ability to model, wind–wave interaction has come a long way since the initial arguments made by Jeffreys (1925). Although large-scale field campaigns have been the driving force in advancing our understanding of air–sea interactions, high-fidelity deterministic numerical simulations are set to play a bigger part in the decades to come. With exascale computing systems becoming available within this decade (2020–30) (Sprague et al. 2017), wave-phase-resolved simulations will become a key instrument to the scientific and engineering communities. Nevertheless, efforts for more accurate wave-phase-averaged and wall-stress parameterizations of wind–wave interactions should continue during this transitional era. Henceforth, large-scale field data will remain a rich source of information going forward.

Acknowledgments. This work was authored by the National Renewable Energy Laboratory (NREL), operated by Alliance for Sustainable Energy, LLC, for the U.S. Department of Energy (DOE) under Contract DE-AC36-08GO28308. Funding was provided by the U.S. Department of Energy Office of Energy Efficiency and Renewable Energy Wind Energy Technologies Office. The views expressed in the article do not necessarily represent the views of the DOE or the U.S. government. The U.S. government retains and the publisher, by accepting the article for publication, acknowledges that the U.S. government retains a nonexclusive, paid-up, irrevocable, worldwide license to publish or reproduce the published form of this work or to allow others to do so, for U.S. government purposes. A portion of the research was performed using computational resources sponsored by the DOE Office of Energy Efficiency and Renewable Energy and located at the National Renewable Energy Laboratory. The authors thank Dr. Matthew Churchfield for his valuable comments during the completion of this work.

APPENDIX

Numerical Implementation of the HOS Method and Further Details on the Wave Field Initialization and Generation

a. *High-order spectral solver*

A common method to solve the Zakharov Eq. (24) is to use a pseudospectral solver (Dommermuth and Yue 1987). That is, some of the operators are treated in the physical domain (e.g., products of quantities), whereas others are treated in the

spectral domain (evaluation of the spatial derivatives). This model is often referred as the HOS model, and it is, in general, characterized by high efficiency and accuracy as compared with low-order spatial discretization codes for wave propagation. The key concept of the method is based on expanding the free-surface velocity potential and vertical velocity in wave steepness, $\varepsilon = (ak)$, up to an order M,

$$\Phi(x,y,z,t) = \sum_{m=1}^{M} \Phi^{(m)}(x,y,z,t) \quad \text{and} \tag{A1a}$$

$$W(x,y,z,t) = \sum_{m=1}^{M} W^{(m)}(x,y,z,t), \tag{A1b}$$

where both $\Phi^{(m)}$ and $W^{(m)}$ are quantities of order ε^m that can be expanded into a Taylor series around $z = 0$ so that

$$\Phi^{(1)}(x,y,0,t) = \Phi_s(x,y,t) \quad \text{and} \tag{A2a}$$

$$\Phi^{(m)}(x,y,0,t) = -\sum \frac{\eta^k}{k!} \frac{\partial^k \Phi^{(m-k)}}{\partial z^k}(x,y,0,t) \quad \text{for} \quad m > 1, \tag{A2b}$$

and, similarly,

$$W^{(m)}(x,y,0,t) = \sum \frac{\eta^k}{k!} \frac{\partial^{k+1} \Phi^{(m-k)}}{\partial z^{k+1}}(x,y,0,t) \quad \text{for} \quad m > 1. \tag{A3}$$

The velocity potentials, $\Phi^{(m)}$, are then expanded using eigenfunctions,

$$\Phi^{(m)} = \sum_{n=1}^{N} \Phi_n^{(m)} \Psi_n(x,y,z), \tag{A4}$$

where, for deep-water waves,

$$\Psi_n(x,y,z) = \frac{\cosh[k(z+h)]}{\cosh(kh)} \exp[i(\mathbf{k}\cdot\mathbf{x})], \tag{A5}$$

and where $\mathbf{k} = [k_x^{(m)}, k_y^{(m)}]$ are the wavenumbers associated with the modal discretization [e.g., $k_x^{(m)} = m\Delta_x = m2\pi/L_x$]. Subsequently, the solution is obtained using a pseudospectral method that enables treating some of the operators in the physical space and others in the spectral space. Further details on the implementation, including dealiasing and time integration of the solution, can be found, for example, in the original work of Dommermuth and Yue (1987) as well as in subsequent algorithmic implementations (Ducrozet et al. 2016).

b. Wave field initialization

Another important aspect of the HOS wave model is the initialization of the sea states. We elaborate here on two initializations of two different sea states, nonlinear regular waves and irregular waves based on directional wave spectra (e.g., JONSWAP). The former follows the method proposed by Rienecker and Fenton (1981), which uses a spectral solution to calculate the nonlinear profile of monochromatic, regular waves for a large range of amplitudes, wave lengths and water depths. The latter uses a directional wave spectrum, $S(\omega, \theta) = G(\theta)F_j(\omega)$, where

$$F(\omega) = \frac{ag^2}{\omega^5} \exp\left[-\frac{5}{4}\left(\frac{\omega_p}{\omega}\right)^4\right]\gamma^r, \tag{B1}$$

where $r = \exp[-(\omega-\omega)^2/(2\sigma^2\omega_p^2)]$ and ω_p is the angular frequency at the peak of the spectrum. The particular JONSWAP spectrum uses $\alpha = 3.279E$, $\gamma = 3.3$, and $\sigma = 0.07$ for $\omega < 1$ and $\sigma = 0.09$ for $\omega \geq 1$, where E is the dimensionless energy density of the wave field. The dimensionless energy density E may also be related to the significant wave height via $H_s \approx 4(E)^{1/2}$. On the other hand, the directional spreading function is defined as

$$G(\theta) = \frac{1}{\beta}\left[\cos\left(\frac{\pi\theta}{2\beta}\right)\right]^2. \tag{B2}$$

To initialize the free-surface elevation according to the wave spectrum, the modal amplitude is defined as

$$\frac{1}{2}|B_{ij}^h|^2 = S(k_x,k_y)\Delta k_x \Delta k_y = \frac{\partial\omega}{\partial k}\frac{1}{k}S(\omega,\theta)\Delta k_x \Delta k_y, \tag{B3}$$

where $\Delta k_x = 2\pi/L_x$ and $\Delta k_y = 2\pi/L_y$ correspond to the modal discretization in the x and y directions and L_x and L_y are the respective domain dimensions. The free-surface potential is linearly evaluated from the elevation, $B_{mn}^{\Phi} = -i\omega_{mn}/gB_{mn}^h$, where ω_{mn} is given by the dispersion function. Another important aspect of the initialization process is using a relaxation period, as pointed out by Dommermuth (2000). As initializing the nonlinear field is achieved through a superposition of linear components, numerical instabilities may arise in the sea state and evolve during the initial transitional period (5–10 periods T_p). To overcome this, Dommermuth (2000) introduced a relaxation scheme that uses the transitional time period T_a to dampen the spurious oscillations

$$\frac{\partial\Phi^S}{\partial t} + gh = \mathscr{F}\{1 - \exp[-(t/T_a)^n]\} \quad \text{and} \tag{B4a}$$

$$\frac{\partial h}{\partial t} - W^{(1)} = \mathscr{G}\{1 - \exp[-(t/T_a)^n]\}, \tag{B4b}$$

where $\mathscr{F}$ and $\mathscr{G}$ are the nonlinear parts of the kinematic and dynamic free-surface boundary conditions formulated in the Zakharov Eqs. (24). The relaxation period and exponent n are usually taken to be $10T_p$ (10 peak periods) and $n = 4$, respectively.

REFERENCES

Airy, G., 1845: *Tides and Waves*. B. Fellowes, 156 pp.

Åkervik, E., and M. Vartdal, 2019: The role of wave kinematics in turbulent flow over waves. *J. Fluid Mech.*, **880**, 890–915, https://doi.org/10.1017/jfm.2019.708.

AlSam, A., R. Szasz, and J. Revstedt, 2015: The influence of sea waves on offshore wind turbine aerodynamics. *J. Energy Resour. Technol.*, **137**, 051209, https://doi.org/10.1115/1.4031005.

Anderson, J., 1995: *Computational Fluid Dynamics: The Basics with Applications*. McGraw-Hill, 547 pp.

Andren, A., A. R. Brown, P. J. Mason, J. Graf, U. Schumann, C. H. Moeng, and F. T. M. Nieuwstadt, 1994: Large-eddy simulation

of a neutrally stratified boundary layer: A comparison of four computer codes. *Quart. J. Roy. Meteor. Soc.*, **120**, 1457–1484, https://doi.org/10.1002/qj.49712052003.

Arthur, R. S., K. A. Lundquist, D. J. Wiersema, J. Bao, and F. K. Chow, 2020: Evaluating implementations of the immersed boundary method in the Weather Research and Forecasting Model. *Mon. Wea. Rev.*, **148**, 2087–2109, https://doi.org/10.1175/MWR-D-19-0219.1.

Bakhoday-Paskyabi, M., I. Fer, and J. Reuder, 2018: Current and turbulence measurements at the FINO1 offshore wind energy site: Analysis using 5-beam ADCPs. *Ocean Dyn.*, **68**, 109–130, https://doi.org/10.1007/s10236-017-1109-5.

Banner, M. L., 1990: Equilibrium spectra of wind waves. *J. Phys. Oceanogr.*, **20**, 966–984, https://doi.org/10.1175/1520-0485(1990)020<0966:ESOWW>2.0.CO;2.

Bao, J., F. K. Chow, and K. A. Lundquist, 2018: Large-eddy simulation over complex terrain using an improved immersed boundary method in the Weather Research and Forecasting Model. *Mon. Wea. Rev.*, **146**, 2781–2797, https://doi.org/10.1175/MWR-D-18-0067.1.

Basu, S., and F. Porté-Agel, 2006: Large-eddy simulation of stably stratified atmospheric boundary layer turbulence: A scale-dependent dynamic modeling approach. *J. Atmos. Sci.*, **63**, 2074–2091, https://doi.org/10.1175/JAS3734.1.

Batchelor, G. K., and I. Proudman, 1954: The effect of rapid distortion of a fluid in turbulent motion. *Quart. J. Mech. Appl. Math.*, **7**, 83–103, https://doi.org/10.1093/qjmam/7.1.83.

Belcher, S. E., and J. C. R. Hunt, 1993: Turbulent shear flow over slowly moving waves. *J. Fluid Mech.*, **251**, 109–148, https://doi.org/10.1017/S0022112093003350.

——, and ——, 1998: Turbulent flow over hills and waves. *Annu. Rev. Fluid Mech.*, **30**, 507–538, https://doi.org/10.1146/annurev.fluid.30.1.507.

Bell, M. M., M. T. Montgomery, and K. A. Emanuel, 2012: Air–sea enthalpy and momentum exchange at major hurricane wind speeds observed during CBLAST. *J. Atmos. Sci.*, **69**, 3197–3222, https://doi.org/10.1175/JAS-D-11-0276.1.

Black, P. G., and Coauthors, 2007: Air–sea exchange in hurricanes: Synthesis of observations from the Coupled Boundary Layer Air–Sea Transfer experiment. *Bull. Amer. Meteor. Soc.*, **88**, 357–374, https://doi.org/10.1175/BAMS-88-3-357.

Bodini, N., J. K. Lundquist, and A. Kirincich, 2019: U.S. East Coast lidar measurements show offshore wind turbines will encounter very low atmospheric turbulence. *Geophys. Res. Lett.*, **46**, 5582–5591, https://doi.org/10.1029/2019GL082636.

Breton, S.-P., J. Sumner, J. N. Sørensen, K. S. Hansen, S. Sarmast, and S. Ivanell, 2017: A survey of modelling methods for high-fidelity wind farm simulations using large eddy simulation. *Philos. Trans. Roy. Soc. London*, **375**, 20160097, https://doi.org/10.1098/rsta.2016.0097.

Buckley, M. P., and F. Veron, 2016: Structure of the airflow above surface waves. *J. Phys. Oceanogr.*, **46**, 1377–1397, https://doi.org/10.1175/JPO-D-15-0135.1.

——, and ——, 2017: Airflow measurements at a wavy air–water interface using PIV and LIF. *Exp. Fluids*, **58**, 161, https://doi.org/10.1007/s00348-017-2439-2.

——, ——, and K. Yousefi, 2020: Surface viscous stress over wind-driven waves with intermittent airflow separation. *J. Fluid Mech.*, **905**, A31, https://doi.org/10.1017/jfm.2020.760.

Butterfield, S., W. Musial, J. Jonkman, and P. Sclavounos, 2007: Engineering challenges for floating offshore wind turbines. NREL Tech. Rep., 13 pp.

Calaf, M., C. Meneveau, and J. Meyers, 2010: Large eddy simulation study of fully developed wind-turbine array boundary layers. *Phys. Fluids*, **22**, 015110, https://doi.org/10.1063/1.3291077.

Calderer, A., X. Guo, L. Shen, and F. Sotiropoulos, 2018: Fluid-structure interaction simulation of floating structures interacting with complex, large-scale ocean waves and atmospheric turbulence with application to floating offshore wind turbines. *J. Comput. Phys.*, **355**, 144–175, https://doi.org/10.1016/j.jcp.2017.11.006.

Cao, T., B.-Q. Deng, and L. Shen, 2020: A simulation-based mechanistic study of turbulent wind blowing over opposing water waves. *J. Fluid Mech.*, **901**, A27, https://doi.org/10.1017/jfm.2020.591.

Cavaleri, L., B. Fox-Kemper, and M. Hemer, 2012: Wind waves in the coupled climate system. *Bull. Amer. Meteor. Soc.*, **93**, 1651–1661, https://doi.org/10.1175/BAMS-D-11-00170.1.

Charnock, H., 1955: Wind stress on a water surface. *Quart. J. Roy. Meteor. Soc.*, **81**, 639–640, https://doi.org/10.1002/qj.49708135027.

Chen, S., F. Qiao, C. J. Huang, and B. Zhao, 2018: Deviation of wind stress from wind direction under low wind conditions. *J. Geophys. Res. Oceans*, **123**, 9357–9368, https://doi.org/10.1029/2018JC014137.

——, ——, Y. Xue, S. Chen, and H. Ma, 2020: Directional characteristic of wind stress vector under swell-dominated conditions. *J. Geophys. Res. Oceans*, **125**, e2020JC016352, https://doi.org/10.1029/2020JC016352.

Chen, S. S., J. F. Price, W. Zhao, M. A. Donelan, and E. J. Walsh, 2007: The CBLAST-Hurricane program and the next-generation fully coupled atmosphere–wave–ocean models for hurricane research and prediction. *Bull. Amer. Meteor. Soc.*, **88**, 311–318, https://doi.org/10.1175/BAMS-88-3-311.

——, W. Zhao, M. A. Donelan, and H. L. Tolman, 2013: Directional wind–wave coupling in fully coupled atmosphere–wave–ocean models: Results from CBLAST-Hurricane. *J. Atmos. Sci.*, **70**, 3198–3215, https://doi.org/10.1175/JAS-D-12-0157.1.

Chow, F. K., A. P. Weigel, R. L. Street, M. W. Rotach, and M. Xue, 2006: High-resolution large-eddy simulations of flow in a steep Alpine valley. Part I: Methodology, verification, and sensitivity experiments. *J. Appl. Meteor. Climatol.*, **45**, 63–86, https://doi.org/10.1175/JAM2322.1.

Churchfield, M. J., S. Lee, P. J. Moriarty, L. A. Martinez, S. Leonardi, G. Vijayakumar, and J. G. Brasseur, 2012: A large-eddy simulation of wind-plant aerodynamics. *50th AIAA Aerospace Sciences Meeting*, Nashville, TN, AIAA, 0537, https://doi.org/10.2514/6.2012-537.

Cohen, J. E., and S. E. Belcher, 1999: Turbulent shear flow over fast-moving waves. *J. Fluid Mech.*, **386**, 345–371, https://doi.org/10.1017/S0022112099004383.

Crescenti, G. H., J. R. French, and T. Crawford, 2001: Aircraft measurements in the Coupled Boundary Layers Air-Sea Transfer (CBLAST) light wind pilot field study. NOAA Tech. Rep., 82 pp.

Csanady, G., and M. Gibson, 2001: *Air-Sea Interaction: Laws and Mechanisms*. Cambridge University Press, 239 pp.

Dean, R., and R. Dalrymple, 1991: *Water Wave Mechanics for Engineers and Scientists*. Advanced Series on Ocean Engineering, Vol. 2, World Scientific, 368 pp.

Deardorff, J. W., 1972: Numerical investigation of neutral and unstable planetary boundary layers. *J. Atmos. Sci.*, **29**, 91–115, https://doi.org/10.1175/1520-0469(1972)029<0091:NIONAU>2.0.CO;2.

DeCosmo, J., K. B. Katsaros, S. D. Smith, R. J. Anderson, W. A. Oost, K. Bumke, and H. Chadwick, 1996: Air-sea exchange of

water vapor and sensible heat: The Humidity Exchange over the Sea (HEXOS) results. *J. Geophys. Res.*, **101**, 12 001–12 016, https://doi.org/10.1029/95JC03796.

DeLeon, R., M. Sandusky, and I. Senocak, 2018: Simulations of turbulent flow over complex terrain using an immersed-boundary method. *Bound.-Layer Meteor.*, **167**, 399–420, https://doi.org/10.1007/s10546-018-0336-8.

Demirdžić, I., and M. Perić, 1990: Finite volume method for prediction of fluid flow in arbitrarily shaped domains with moving boundaries. *Int. J. Numer. Methods Fluids*, **10**, 771–790, https://doi.org/10.1002/fld.1650100705.

Deskos, G., S. Laizet, and R. Palacios, 2020: WInc3D: A novel framework for turbulence-resolving simulations of wind farm wake interactions. *Wind Energy*, **23**, 779–794, https://doi.org/10.1002/we.2458.

Diebold, M., C. Higgins, J. Fang, A. Bechmann, and M. B. Parlange, 2013: Flow over hills: A large-eddy simulation of the Bolund case. *Bound.-Layer Meteor.*, **148**, 177–194, https://doi.org/10.1007/s10546-013-9807-0.

Dommermuth, D., 2000: The initialization of nonlinear waves using an adjustment scheme. *Wave Motion*, **32**, 307–317, https://doi.org/10.1016/S0165-2125(00)00047-0.

——, and D. K. P. Yue, 1987: A high-order spectral method for the study of nonlinear gravity waves. *J. Fluid Mech.*, **184**, 267–288, https://doi.org/10.1017/S002211208700288X.

Donéa, J., S. Giuliani, and J. P. Halleux, 1982: An arbitrary Lagrangian-Eulerian finite element method for transient dynamic fluid-structure interactions. *Comput. Methods Appl. Mech. Eng.*, **33**, 689–723, https://doi.org/10.1016/0045-7825(82)90128-1.

Donelan, M. A., 1990: Air-sea interaction. *Ocean Engineering Science*, Vol. 9B, *The Sea—Ideas and Observations on Progress in the Study of the Seas*, B. LeMehaute and D. M. Hanes, Eds., John Wiley and Sons, 239–292.

——, 2018: On the decrease of the oceanic drag coefficient in high winds. *J. Geophys. Res. Oceans*, **123**, 1485–1501, https://doi.org/10.1002/2017JC013394.

——, J. Hamilton, and W. H. Hui, 1985: Directional spectra of wind-generated ocean waves. *Philos. Trans. Roy. Soc. London*, **315**, 509–562, https://doi.org/10.1098/rsta.1985.0054.

——, W. M. Drennan, and K. B. Katsaros, 1997: The air–sea momentum flux in conditions of wind sea and swell. *J. Phys. Oceanogr.*, **27**, 2087–2099, https://doi.org/10.1175/1520-0485(1997)027<2087:TASMFI>2.0.CO;2.

Drennan, W. M., H. C. Graber, D. Hauser, and C. Quentin, 2003: On the wave age dependence of wind stress over pure wind seas. *J. Geophys. Res.*, **108**, 8062, https://doi.org/10.1029/2000JC000715.

——, P. K. Taylor, and M. J. Yelland, 2005: Parameterizing the sea surface roughness. *J. Phys. Oceanogr.*, **35**, 835–848, https://doi.org/10.1175/JPO2704.1.

——, J. A. Zhang, J. R. French, C. McCormick, and P. G. Black, 2007: Turbulent fluxes in the hurricane boundary layer. Part II: Latent heat flux. *J. Atmos. Sci.*, **64**, 1103–1115, https://doi.org/10.1175/JAS3889.1.

Druzhinin, O. A., Y. I. Troitskaya, and S. S. Zilitinkevich, 2012: Direct numerical simulation of a turbulent wind over a wavy water surface. *J. Geophys. Res.*, **117**, C00J05, https://doi.org/10.1029/2011JC007789.

Ducrozet, G., F. Bonnefoy, D. L. Touzé, and P. Ferrant, 2016: HOS-ocean: Open-source solver for nonlinear waves in open ocean based on high-order spectral method. *Comput. Phys. Commun.*, **203**, 245–254, https://doi.org/10.1016/j.cpc.2016.02.017.

Dunckel, M., L. Hasse, L. Krügermeyer, D. Schriever, and J. Wucknitz, 1974: Turbulent fluxes of momentum, heat and water vapor in the atmospheric surface layer at sea during ATEX. *Bound.-Layer Meteor.*, **6**, 81–106, https://doi.org/10.1007/BF00232478.

Edson, J., and Coauthors, 2007: The Coupled Boundary Layers and Air–Sea Transfer experiment in low winds. *Bull. Amer. Meteor. Soc.*, **88**, 341–356, https://doi.org/10.1175/BAMS-88-3-341.

——, and Coauthors, 2013: On the exchange of momentum over the open ocean. *J. Phys. Oceanogr.*, **43**, 1589–1610, https://doi.org/10.1175/JPO-D-12-0173.1.

EERE, 2020: EERE funding opportunity exchange. U.S. DOE, https://eere-exchange.energy.gov/.

Elfouhaily, T., B. Chapron, K. Katsaros, and D. Vandemark, 1997: A unified directional spectrum for long and short wind-driven waves. *J. Geophys. Res.*, **102**, 15 781–15 796, https://doi.org/10.1029/97JC00467.

Fairall, C. W., E. F. Bradley, J. E. Hare, A. A. Grachev, and J. B. Edson, 2003: Bulk parameterization of air–sea fluxes: Updates and verification for the COARE algorithm. *J. Climate*, **16**, 571–591, https://doi.org/10.1175/1520-0442(2003)016<0571:BPOASF>2.0.CO;2.

Fedorovich, E., 1986: Numerical modelling of atmospheric boundary layer flow over topography elements. Ph.D. thesis, Voeikov Main Geophysical Observatory.

Fenton, J., 1985: Fifth order stokes theory for steady waves. *J. Waterw. Port Coastal Ocean Eng.*, **111**, 216–234, https://doi.org/10.1061/(ASCE)0733-950X(1985)111:2(216).

Filippelli, M. V., M. Markus, M. Eberhard, B. H. Bailey, and L. Dubois, 2015: Metocean data needs assessment and data collection strategy development for the Massachusetts Wind Energy Area. AWS Truepower Tech. Rep., 98 pp.

Fischer, G., 2006: Installation and operation of the research platform FINO1 in the North Sea. *Offshore Wind Energy: Research on Environmental Impacts*, J. Köller, J. Köppel, and W. Peters, Eds., Springer, 237–253.

Fischer, J., C. Senet, O. Outzen, A. Schneehorst, and K. Herklotz, 2012: Regional oceanographic distinctions in the south-eastern part of the North Sea: Results of two years of monitoring at the research platforms FINO1 and FINO3. *11th German Wind Energy Conf.*, Bremen, Germany, DEWEK.

Foreman, R. J., and S. Emeis, 2010: Revisiting the definition of the drag coefficient in the marine atmospheric boundary layer. *J. Phys. Oceanogr.*, **40**, 2325–2332, https://doi.org/10.1175/2010JPO4420.1.

French, J. R., W. M. Drennan, J. A. Zhang, and P. G. Black, 2007: Turbulent fluxes in the hurricane boundary layer. Part I: Momentum flux. *J. Atmos. Sci.*, **64**, 1089–1102, https://doi.org/10.1175/JAS3887.1.

Garratt, J. R., 1977: Review of drag coefficients over oceans and continents. *Mon. Wea. Rev.*, **105**, 915–929, https://doi.org/10.1175/1520-0493(1977)105<0915:RODCOO>2.0.CO;2.

Geernaert, G., 1990: Bulk parameterizations for the wind stress and heat fluxes. *Surface Waves and Fluxes*, G. L. Geernaert and W. J. Plant, Eds., Springer, 91–172.

——, K. B. Katsaros, and K. Richter, 1986: Variation of the drag coefficient and its dependence on sea state. *J. Geophys. Res.*, **91**, 7667–7679, https://doi.org/10.1029/JC091iC06p07667.

——, S. E. Larsen, and F. Hansen, 1987: Measurements of the wind stress, heat flux, and turbulence intensity during storm conditions over the North Sea. *J. Geophys. Res.*, **92**, 13 127–13 139, https://doi.org/10.1029/JC092iC12p13127.

Grachev, A. A., and C. W. Fairall, 2001: Upward momentum transfer in the marine boundary layer. *J. Phys. Oceanogr.*, **31**, 1698–1711, https://doi.org/10.1175/1520-0485(2001)031<1698:UMTITM>2.0.CO;2.

——, ——, J. E. Hare, J. B. Edson, and S. D. Miller, 2003: Wind stress vector over ocean waves. *J. Phys. Oceanogr.*, **33**, 2408–2429, https://doi.org/10.1175/1520-0485(2003)033<2408:WSVOOW>2.0.CO;2.

Grare, L., L. Lenain, and W. K. Melville, 2013: Wave-coherent airflow and critical layers over ocean waves. *J. Phys. Oceanogr.*, **43**, 2156–2172, https://doi.org/10.1175/JPO-D-13-056.1.

——, ——, and ——, 2018: Vertical profiles of the wave-induced airflow above ocean surface waves. *J. Phys. Oceanogr.*, **48**, 2901–2922, https://doi.org/10.1175/JPO-D-18-0121.1.

Griffith, B. E., and N. A. Patankar, 2020: Immersed methods for fluid–structure interaction. *Annu. Rev. Fluid Mech.*, **52**, 421–448, https://doi.org/10.1146/annurev-fluid-010719-060228.

Hallgren, C., J. Arnqvist, S. Ivanell, H. Körnich, V. Vakkari, and E. Sahlée, 2020: Looking for an offshore low-level jet champion among recent reanalyses: A tight race over the Baltic Sea. *Energies*, **13**, 3670, https://doi.org/10.3390/en13143670.

Hao, X., and L. Shen, 2019: Wind-wave coupling study using LES of wind and phase-resolved simulation of nonlinear waves. *J. Fluid Mech.*, **874**, 391–425, https://doi.org/10.1017/jfm.2019.444.

——, T. Cao, Z. Yang, T. Li, and L. Shen, 2018: Simulation-based study of wind-wave interaction. *Procedia IUTAM*, **26**, 162–173, https://doi.org/10.1016/j.piutam.2018.03.016.

Hara, T., and P. P. Sullivan, 2015: Wave boundary layer turbulence over surface waves in a strongly forced condition. *J. Phys. Oceanogr.*, **45**, 868–883, https://doi.org/10.1175/JPO-D-14-0116.1.

Hsu, C.-T., and E. Y. Hsu, 1983: On the structure of turbulent flow over a progressive water wave: Theory and experiment in a transformed wave-following coordinate system. Part 2. *J. Fluid Mech.*, **131**, 123–153, https://doi.org/10.1017/S0022112083001263.

——, ——, and R. L. Street, 1981: On the structure of turbulent flow over a progressive water wave: Theory and experiment in a transformed, wave-following co-ordinate system. *J. Fluid Mech.*, **105**, 87–117, https://doi.org/10.1017/S0022112081003121.

Hunt, J., and S. Sajjadi, 2003: Preface. *Wind over Waves II*, S. G. Sajjadi and L. J. Hunt, Eds., Woodhead Publishing, iii–viii.

Husain, N. T., T. Hara, M. P. Buckley, K. Yousefi, F. Veron, and P. P. Sullivan, 2019: Boundary layer turbulence over surface waves in a strongly forced condition: LES and observation. *J. Phys. Oceanogr.*, **49**, 1997–2015, https://doi.org/10.1175/JPO-D-19-0070.1.

IEC, 2009a: Wind turbines—Part 1: Design requirements. IEC International Standard IEC-61400-1, 92 pp.

——, 2009b: Wind turbines—Part 3: Design requirements for offshore wind turbines. IEC International Standard IEC-61400-3, 263 pp.

Janssen, P. A. E. M., 1989: Wave-induced stress and the drag of air flow over sea waves. *J. Phys. Oceanogr.*, **19**, 745–754, https://doi.org/10.1175/1520-0485(1989)019<0745:WISATD>2.0.CO;2.

——, 1991: Quasi-linear theory of wind-wave generation applied to wave forecasting. *J. Phys. Oceanogr.*, **21**, 1631–1642, https://doi.org/10.1175/1520-0485(1991)021<1631:QLTOWW>2.0.CO;2.

——, 2004: *The Interaction of Ocean Waves and Wind*. Cambridge University Press, 312 pp.

Jeffreys, H., 1925: On the formation of water waves by wind. *Proc. Roy. Soc. London*, **107**, 189–206, https://doi.org/10.1098/rspa.1925.0015.

Jiang, Q., P. Sullivan, S. Wang, J. Doyle, and L. Vincent, 2016: Impact of swell on air–sea momentum flux and marine boundary layer under low-wind conditions. *J. Atmos. Sci.*, **73**, 2683–2697, https://doi.org/10.1175/JAS-D-15-0200.1.

Jiménez, P. A., and J. Dudhia, 2018: On the need to modify the sea surface roughness formulation over shallow waters. *J. Appl. Meteor. Climatol.*, **57**, 1101–1110, https://doi.org/10.1175/JAMC-D-17-0137.1.

Johnson, H. K., J. Højstrup, H. J. Vested, and S. E. Larsen, 1998: On the dependence of sea surface roughness on wind waves. *J. Phys. Oceanogr.*, **28**, 1702–1716, https://doi.org/10.1175/1520-0485(1998)028<1702:OTDOSS>2.0.CO;2.

Jones, I. S. F., and Y. Toba, 2001: *Wind Stress over the Ocean*. Cambridge University Press, 307 pp.

Jonkman, J., S. Butterfield, W. Musial, and G. Scott, 2009: Definition of a 5-MW reference wind turbine for offshore system development. NREL Tech. Rep., 75 pp.

Kaimal, J. C., and J. Finnigan, 1994: *Atmospheric Boundary Layer Flows*. Oxford University Press, 304 pp.

Karaki, S., and E. Y. Hsu, 1968: An experimental investigation of the structure of a turbulent wind over water waves. Stanford University Dept. of Civil Engineering Tech. Rep. 88, 121 pp.

Kihara, N., H. Hanazaki, T. Mizuya, and H. Ueda, 2007: Relationship between airflow at the critical height and momentum transfer to the traveling waves. *Phys. Fluids*, **19**, 015102, https://doi.org/10.1063/1.2409736.

Kim, E., L. Manuel, M. Curcic, S. S. Chen, C. Phillips, and P. Veers, 2016: On the use of coupled wind, wave, and current fields in the simulation of loads on bottom-supported offshore wind turbines during hurricanes: March 2012–September 2015. NREL Tech. Rep., 188 pp.

Kitaigorodskii, S., 1968: On the calculation of aerodynamic roughness of the sea surface. *Izv. Akad. Sci. SSSR Atmos. Oceanic Phys.*, **4**, 498–502.

——, 1973: *The Physics of Air-Sea Interaction*. Israel Program for Scientific Translations, 237 pp.

——, and Y. A. Volkov, 1965: On the roughness parameter of the sea surface and the calculation of momentum flux in the near water layer of the atmosphere. *Izv. Acad. Sci. SSSR Atmos. Oceanic Phys.*, **1**, 973–988.

Kosović, B., and J. A. Curry, 2000: A large eddy simulation study of a quasi-steady, stably stratified atmospheric boundary layer. *J. Atmos. Sci.*, **57**, 1052–1068, https://doi.org/10.1175/1520-0469(2000)057<1052:ALESSO>2.0.CO;2.

Lange, B., H. K. Johnson, S. Larsen, J. Højstrup, H. Kofoed-Hansen, and M. J. Yelland, 2004: On detection of a wave age dependency for the sea surface roughness. *J. Phys. Oceanogr.*, **34**, 1441–1458, https://doi.org/10.1175/1520-0485(2004)034<1441:ODOAWA>2.0.CO;2.

Li, F., W. Large, W. Shaw, K. Davidson, and E. J. Walsh, 1989: Ocean radar backscatter relationship with near-surface winds: A case study during FASINEX. *J. Phys. Oceanogr.*, **19**, 342–353, https://doi.org/10.1175/1520-0485(1989)019<0342:ORBRWN>2.0.CO;2.

Li, P. Y., D. Xu, and P. A. Taylor, 2000: Numerical modelling of turbulent airflow over water waves. *Bound.-Layer Meteor.*, **95**, 397–425, https://doi.org/10.1023/A:1002677312259.

Li, Q., E. Bou-Zeid, N. Vercauteren, and M. Parlange, 2018: Signatures of air–wave interactions over a large lake. *Bound.-Layer Meteor.*, **167**, 445–468, https://doi.org/10.1007/s10546-017-0329-z.

Li, X. M., and S. Lehner, 2013: Observation of TerraSAR-X for studies on offshore wind turbine wake in near and far fields.

IEEE J. Sel. Top. Appl. Earth Obs. Remote Sens., **6**, 1757–1768, https://doi.org/10.1109/JSTARS.2013.2263577.

Lin, M.-Y., C.-H. Moeng, W.-T. Tsai, P. P. Sullivan, and S. Belcher, 2008: Direct numerical simulation of wind-wave generation processes. *J. Fluid Mech.*, **616**, 1–30, https://doi.org/10.1017/S0022112008004060.

Liu, L., and R. J. Stevens, 2020: Wall modeled immersed boundary method for high Reynolds number flow over complex terrain. *Comput. Fluids*, **208**, 104604, https://doi.org/10.1016/j.compfluid.2020.104604.

Liu, Y., D. Yang, X. Guo, and L. Shen, 2010: Numerical study of pressure forcing of wind on dynamically evolving water waves. *Phys. Fluids*, **22**, 041704, https://doi.org/10.1063/1.3414832.

Longuet-Higgins, M. S., and E. D. Cokelet, 1976: The deformation of steep surface waves on water. I. A numerical method of computation. *Proc. Roy. Soc. London*, **350**, 1–26, https://doi.org/10.1098/rspa.1976.0092.

Ma, Q., and S. Yan, 2006: Quasi ALE finite element method for nonlinear water waves. *J. Comput. Phys.*, **212**, 52–72, https://doi.org/10.1016/j.jcp.2005.06.014.

Ma, Y., and H. Liu, 2017: Large-eddy simulations of atmospheric flows over complex terrain using the immersed-boundary method in the Weather Research and Forecasting Model. *Bound.-Layer Meteor.*, **165**, 421–445, https://doi.org/10.1007/s10546-017-0283-9.

Makin, V. K., and V. N. Kudryavtsev, 1999: Coupled sea surface-atmosphere model: 1. Wind over waves coupling. *J. Geophys. Res.*, **104**, 7613–7623, https://doi.org/10.1029/1999JC900006.

Mason, P. J., 1988: Large-eddy simulation of the convective atmospheric boundary layer. *J. Atmos. Sci.*, **46**, 1492–1516, https://doi.org/10.1175/1520-0469(1989)046<1492:LESOTC>2.0.CO;2.

——, and D. J. Thomson, 1987: Large-eddy simulations of the neutral-static-stability planetary boundary layer. *Quart. J. Roy. Meteor. Soc.*, **113**, 413–443, https://doi.org/10.1002/qj.49711347602.

——, and S. H. Derbyshire, 1990: Large-eddy simulation of the stably-stratified atmospheric boundary layer. *Bound.-Layer Meteor.*, **53**, 117–162, https://doi.org/10.1007/BF00122467.

Mastenbroek, C., 1996: Wind–wave interaction. Ph.D. thesis, Technische Universiteit Delft, 117 pp.

——, V. K. Makin, M. H. Garat, and J. P. Giovanangeli, 1996: Experimental evidence of the rapid distortion of turbulence in the air flow over water waves. *J. Fluid Mech.*, **318**, 273–302, https://doi.org/10.1017/S0022112096007124.

Masuda, A., and T. Kusaba, 1987: On the local equilibrium of winds and wind-waves in relation to surface drag. *J. Oceanogr. Soc. Japan*, **43**, 28–36, https://doi.org/10.1007/BF02110631.

Mavriplis, D. J., and Z. Yang, 2006: Construction of the discrete geometric conservation law for high-order time-accurate simulations on dynamic meshes. *J. Comput. Phys.*, **213**, 557–573, https://doi.org/10.1016/j.jcp.2005.08.018.

Meneveau, C., and J. Katz, 2000: Scale-invariance and turbulence models for large-eddy simulation. *Annu. Rev. Fluid Mech.*, **32**, 1–32, https://doi.org/10.1146/annurev.fluid.32.1.1.

Miles, J. W., 1957: On the generation of surface waves by shear flows. *J. Fluid Mech.*, **3**, 185–204, https://doi.org/10.1017/S0022112057000567.

——, 1959a: On the generation of surface waves by shear flows. Part 2. *J. Fluid Mech.*, **6**, 568–582, https://doi.org/10.1017/S0022112059000830.

——, 1959b: On the generation of surface waves by shear flows. Part 3. Kelvin-Helmholtz instability. *J. Fluid Mech.*, **6**, 583–598, https://doi.org/10.1017/S0022112059000842.

——, 1962: On the generation of surface waves by shear flows. Part 4. *J. Fluid Mech.*, **13**, 433–448, https://doi.org/10.1017/S0022112062000828.

——, 1967: On the generation of surface waves by shear flows. Part 5. *J. Fluid Mech.*, **30**, 163–175, https://doi.org/10.1017/S0022112067001351.

——, 1993: Surface-wave generation revisited. *J. Fluid Mech.*, **256**, 427–441, https://doi.org/10.1017/S0022112093002836.

Mitsuta, Y., 1979: Collected scientific papers of the AMTEX. Japanese National Committee for GARP and Disaster Prevention Research Institute Papers, 181 pp.

Mittal, R., and G. Iaccarino, 2005: Immersed boundary methods. *Annu. Rev. Fluid Mech.*, **37**, 239–261, https://doi.org/10.1146/annurev.fluid.37.061903.175743.

Moeng, C.-H., 1984: A large-eddy-simulation model for the study of planetary boundary-layer turbulence. *J. Atmos. Sci.*, **41**, 2052–2062, https://doi.org/10.1175/1520-0469(1984)041<2052:ALESMF>2.0.CO;2.

——, and P. P. Sullivan, 1994: A comparison of shear- and buoyancy-driven planetary boundary layer flows. *J. Atmos. Sci.*, **51**, 999–1022, https://doi.org/10.1175/1520-0469(1994)051<0999:ACOSAB>2.0.CO;2.

Monin, A. S., and A. Obukhov, 1954: Basic laws of turbulent mixing in the atmosphere near the ground. *Tr. Geofiz. Inst., Akad. Nauk SSSR*, **24**, 163–187.

Muñoz-Esparza, D., B. Cañadillas, T. Neumann, and J. Van Beeck, 2012: Turbulent fluxes, stability and shear in the offshore environment: Mesoscale modelling and field observations at FINO1. *J. Renewable Sustainable Energy*, **4**, 063136, https://doi.org/10.1063/1.4769201.

Musial, W., P. Beiter, P. Spitsen, and J. N. V. Gevorgian, 2019: 2018 offshore wind technologies market report. U.S. DOE Tech. Rep., 92 pp.

Newman, J., 1977: *Marine Hydrodynamics*. MIT Press, 402 pp.

Nilsson, E. O., A. Rutgersson, A.-S. Smedman, and P. P. Sullivan, 2012: Convective boundary-layer structure in the presence of wind-following swell. *Quart. J. Roy. Meteor. Soc.*, **138**, 1476–1489, https://doi.org/10.1002/qj.1898.

Nilsson, K., S. Ivanell, K. S. Hansen, R. Mikkelsen, J. N. Sørensen, S.-P. Breton, and D. Henningson, 2015: Large-eddy simulations of the Lillgrund wind farm. *Wind Energy*, **18**, 449–467, https://doi.org/10.1002/we.1707.

Noh, W. F., 1963: CEL: A time-dependent, two-space-dimensional, coupled Eulerian-Lagrange code. Lawrence Radiation Laboratory Rep. UCRL-7463, 76 pp., https://doi.org/10.2172/4621975.

Oost, W. A., G. J. Komen, C. M. J. Jacobs, and C. Van Oort, 2002: New evidence for a relation between wind stress and wave age from measurements during ASGAMAGE. *Bound.-Layer Meteor.*, **103**, 409–438, https://doi.org/10.1023/A:1014913624535.

Patton, E. G., P. P. Sullivan, B. Kosović, J. Dudhia, L. Mahrt, M. Žagar, and T. Marić, 2019: On the influence of swell propagation angle on surface drag. *J. Appl. Meteor. Climatol.*, **58**, 1039–1059, https://doi.org/10.1175/JAMC-D-18-0211.1.

Pedersen, J. G., S.-E. Gryning, and M. Kelly, 2014: On the structure and adjustment of inversion-capped neutral atmospheric boundary-layer flows: Large-eddy simulation study. *Bound.-Layer Meteor.*, **153**, 43–62, https://doi.org/10.1007/s10546-014-9937-z.

Peskin, C. S., 1972: Flow patterns around heart valves: A numerical method. *J. Comput. Phys.*, **10**, 252–271, https://doi.org/10.1016/0021-9991(72)90065-4.

Phillips, O., and Coauthors, 1966: *The Dynamics of the Upper Ocean*. Cambridge University Press, 269 pp.

Pollard, R. T., T. H. Guymer, and P. K. Taylor, 1983: Summary of the JASIN 1978 field experiment. *Philos. Trans. Roy. Soc. London*, **308**, 221–230, https://doi.org/10.1098/rsta.1983.0001.

Porchetta, S., O. Temel, D. Muñoz Esparza, J. Reuder, J. Monbaliu, J. van Beeck, and N. van Lipzig, 2019: A new roughness length parameterization accounting for wind–wave (mis)alignment. *Atmos. Chem. Phys.*, **19**, 6681–6700, https://doi.org/10.5194/acp-19-6681-2019.

——, ——, J. Warner, D. Muñoz-Esparza, J. Monbaliu, J. van Beeck, and N. van Lipzig, 2021: Evaluation of a roughness length parametrization accounting for wind–wave alignment in a coupled atmosphere–wave model. *Quart. J. Roy. Meteor. Soc.*, **147**, 825–846, https://doi.org/10.1002/qj.3948.

Prosperetti, A., and G. Tryggvason, 2009: *Computational Methods for Multiphase Flow*. Cambridge University Press, 488 pp.

Rieder, K. F., J. A. Smith, and R. A. Weller, 1994: Observed directional characteristics of the wind, wind stress, and surface waves on the open ocean. *J. Geophys. Res.*, **99**, 22 589–22 596, https://doi.org/10.1029/94JC02215.

Rienecker, M. M., and J. D. Fenton, 1981: A Fourier approximation method for steady water waves. *J. Fluid Mech.*, **104**, 119–137, https://doi.org/10.1017/S0022112081002851.

Schumann, U., 1975: Subgrid scale model for finite difference simulations of turbulent flows in plane channels and annuli. *J. Comput. Phys.*, **18**, 376–404, https://doi.org/10.1016/0021-9991(75)90093-5.

Senet, C., J. Fischer, O. Outzen, K. Herklotz, and H. Klein, 2012: Remote sensing and in situ sea state instrument comparisons at the research platform FINO1 in the German Bight. *International Geoscience and Remote Sensing Symp.*, Munich, Germany, IEEE, 7625–7628, https://doi.org/10.1109/IGARSS.2012.6351862.

Shen, L., X. Zhang, D. K. P. Yue, and M. S. Triantafyllou, 2003: Turbulent flow over a flexible wall undergoing a streamwise travelling wave motion. *J. Fluid Mech.*, **484**, 197–221, https://doi.org/10.1017/S0022112003004294.

Sjöberg, S., T. Alerstam, S. Åkesson, A. Schulz, A. Weidauer, T. Coppack, and R. Muheim, 2015: Weather and fuel reserves determine departure and flight decisions in passerines migrating across the Baltic Sea. *Anim. Behav.*, **104**, 59–68, https://doi.org/10.1016/j.anbehav.2015.02.015.

Skamarock, W. C., and Coauthors, 2019: A description of the Advanced Research WRF Model version 4. NCAR Tech. Note NCAR/TN-556+STR, 162 pp.

Smagorinsky, J., 1963: General circulation experiments with the primitive equations. *Mon. Wea. Rev.*, **91**, 99–164, https://doi.org/10.1175/1520-0493(1963)091<0099:GCEWTP>2.3.CO;2.

Smedman, A., U. Högström, H. Bergström, A. Rutgersson, K. K. Kahma, and H. Pettersson, 1999: A case study of air-sea interaction during swell conditions. *J. Geophys. Res.*, **104**, 25 833–25 851, https://doi.org/10.1029/1999JC900213.

Smith, C. M., and E. D. Skyllingstad, 2005: Numerical simulation of katabatic flow with changing slope angle. *Mon. Wea. Rev.*, **133**, 3065–3080, https://doi.org/10.1175/MWR2982.1.

Smith, S. D., 1988: Coefficients for sea surface wind stress, heat flux, and wind profiles as a function of wind speed and temperature. *J. Geophys. Res.*, **93**, 15 467–15 472, https://doi.org/10.1029/JC093iC12p15467.

——, and Coauthors, 1992: Sea surface wind stress and drag coefficients: The HEXOS results. *Bound.-Layer Meteor.*, **60**, 109–142, https://doi.org/10.1007/BF00122064.

Sprague, M., S. Boldyrev, P. Fischer, R. Grout, W. I. Gustafson Jr., and R. Moser, 2017: Turbulent flow simulation at exascale: Opportunities and challenges workshop. NREL Tech. Rep. TP-2C00-67648, 68 pp.

——, S. Ananthan, G. Vijayakumar, and M. Robinson, 2020: ExaWind: A multifidelity modeling and simulation environment for wind energy. *J. Phys.*, **1452**, 012071, https://doi.org/10.1088/1742-6596/1452/1/012071.

Stewart, R. E., R. W. Shaw, and G. A. Isaac, 1987: Canadian Atlantic Storms Program: The meteorological field project. *Bull. Amer. Meteor. Soc.*, **68**, 338–345, https://doi.org/10.1175/1520-0477(1987)068<0338:CASPTM>2.0.CO;2.

Stewart, R. H., 1970: Laboratory studies of the velocity field over deep-water waves. *J. Fluid Mech.*, **42**, 733–754, https://doi.org/10.1017/S0022112070001581.

Stokes, G., 1847: On the theory of oscillatory waves. *Trans. Cambridge Philos. Soc.*, **8**, 197–229, https://doi.org/10.1017/CBO9780511702242.013.

Stull, R., 1988: *An Introduction to Boundary Layer Meteorology*. Springer, 670 pp.

Sullivan, P. P., and J. C. McWilliams, 2002: Turbulent flow over water waves in the presence of stratification. *Phys. Fluids*, **14**, 1182–1195, https://doi.org/10.1063/1.1447915.

——, and ——, 2010: Dynamics of winds and currents coupled to surface waves. *Annu. Rev. Fluid Mech.*, **42**, 19–42, https://doi.org/10.1146/annurev-fluid-121108-145541.

——, ——, and C.-H. Moeng, 2000: Simulation of turbulent flow over idealized water waves. *J. Fluid Mech.*, **404**, 47–85, https://doi.org/10.1017/S0022112099006965.

——, J. B. Edson, T. Hristov, and J. C. McWilliams, 2008: Large-eddy simulations and observations of atmospheric marine boundary layers above nonequilibrium surface waves. *J. Atmos. Sci.*, **65**, 1225–1245, https://doi.org/10.1175/2007JAS2427.1.

——, J. C. McWilliams, and E. G. Patton, 2014: Large-eddy simulation of marine atmospheric boundary layers above a spectrum of moving waves. *J. Atmos. Sci.*, **71**, 4001–4027, https://doi.org/10.1175/JAS-D-14-0095.1.

——, M. L. Banner, R. P. Morison, and W. L. Peirson, 2018a: Impacts of wave age on turbulent flow and drag of steep waves. *Procedia IUTAM*, **26**, 174–183, https://doi.org/10.1016/j.piutam.2018.03.017.

——, ——, ——, and ——, 2018b: Turbulent flow over steep steady and unsteady waves under strong wind forcing. *J. Phys. Oceanogr.*, **48**, 3–27, https://doi.org/10.1175/JPO-D-17-0118.1.

Tangvald, B., 2012: Comparison of offshore wind profiles using FINO-1 and FINO-3 data. Ph.D. thesis, University of Stavanger, 58 pp.

Taylor, P. K., and M. J. Yelland, 2001: The dependence of sea surface roughness on the height and steepness of the waves. *J. Phys. Oceanogr.*, **31**, 572–590, https://doi.org/10.1175/1520-0485(2001)031<0572:TDOSSR>2.0.CO;2.

Thomas, P. D., and C. K. Lombard, 1979: Geometric conservation law and its application to flow computations on moving grids. *AIAA J.*, **17**, 1030–1037, https://doi.org/10.2514/3.61273.

Toba, Y., N. Iida, H. Kawamura, N. Ebuchi, and I. S. F. Jones, 1990: Wave dependence of sea-surface wind stress. *J. Phys. Oceanogr.*, **20**, 705–721, https://doi.org/10.1175/1520-0485(1990)020<0705:WDOSSW>2.0.CO;2.

Troitskaya, Y. I., D. A. Sergeev, A. A. Kandaurov, G. A. Baidakov, M. A. Vdovin, and V. I. Kazakov, 2012: Laboratory and theoretical modeling of air-sea momentum transfer under severe wind conditions. *J. Geophys. Res.*, **117**, C00J21, https://doi.org/10.1029/2011JC007778.

Veers, P., and Coauthors, 2019: Grand challenges in the science of wind energy. *Science*, **366**, eaau2027, https://doi.org/10.1126/science.aau2027.

Wang, L.-H., W.-Y. Zhang, X. Hao, W.-X. Huang, L. Shen, C.-X. Xu, and Z. Zhang, 2020: Surface wave effects on energy transfer in overlying turbulent flow. *J. Fluid Mech.*, **893**, A21, https://doi.org/10.1017/jfm.2020.246.

Webster, P. J., and R. Lukas, 1992: TOGA COARE: The Coupled Ocean–Atmosphere Response Experiment. *Bull. Amer. Meteor. Soc.*, **73**, 1377–1416, https://doi.org/10.1175/1520-0477(1992)073<1377:TCTCOR>2.0.CO;2.

Wikle, C. K., R. F. Milliff, and W. G. Large, 1999: Surface wind variability on spatial scales from 1 to 1000 km observed during TOGA COARE. *J. Atmos. Sci.*, **56**, 2222–2231, https://doi.org/10.1175/1520-0469(1999)056<2222:SWVOSS>2.0.CO;2.

Wu, J., 1980: Wind-stress coefficients over sea surface near neutral conditions—A revisit. *J. Phys. Oceanogr.*, **10**, 727–740, https://doi.org/10.1175/1520-0485(1980)010<0727:WSCOSS>2.0.CO;2.

Wu, Y.-T., and F. Porté-Agel, 2015: Modeling turbine wakes and power losses within a wind farm using LES: An application to the Horns Rev offshore wind farm. *Renewable Energy*, **75**, 945–955, https://doi.org/10.1016/j.renene.2014.06.019.

Wyngaard, J. C., 2010: *Turbulence in the Atmosphere*. Cambridge University Press, 316 pp.

Yang, D., and L. Shen, 2009: Characteristics of coherent vortical structures in turbulent flows over progressive surface waves. *Phys. Fluids*, **21**, 125106, https://doi.org/10.1063/1.3275851.

——, and ——, 2010: Direct-simulation-based study of turbulent flow over various waving boundaries. *J. Fluid Mech.*, **650**, 131–180, https://doi.org/10.1017/S0022112009993557.

——, and ——, 2011a: Simulation of viscous flows with undulatory boundaries. Part I: Basic solver. *J. Comput. Phys.*, **230**, 5488–5509, https://doi.org/10.1016/j.jcp.2011.02.036.

——, and ——, 2011b: Simulation of viscous flows with undulatory boundaries: Part II. Coupling with other solvers for two-fluid computations. *J. Comput. Phys.*, **230**, 5510–5531, https://doi.org/10.1016/j.jcp.2011.02.035.

——, C. Meneveau, and L. Shen, 2013a: Dynamic modelling of sea-surface roughness for large-eddy simulation of wind over ocean wavefield. *J. Fluid Mech.*, **726**, 62–99, https://doi.org/10.1017/jfm.2013.215.

——, L. Shen, and C. Meneveau, 2013b: An assessment of dynamic subgrid-scale sea-surface roughness models. *Flow Turbul. Combust.*, **91**, 541–563, https://doi.org/10.1007/s10494-013-9459-7.

——, C. Meneveau, and L. Shen, 2014a: Effect of downwind swells on offshore wind energy harvesting—A large-eddy simulation study. *Renewable Energy*, **70**, 11–23, https://doi.org/10.1016/j.renene.2014.03.069.

——, ——, and ——, 2014b: Large-eddy simulation of offshore wind farm. *Phys. Fluids*, **26**, 025101, https://doi.org/10.1063/1.4863096.

Yang, Z., B.-Q. Deng, and L. Shen, 2018: Direct numerical simulation of wind turbulence over breaking waves. *J. Fluid Mech.*, **850**, 120–155, https://doi.org/10.1017/jfm.2018.466.

Yousefi, K., F. Veron, and M. P. Buckley, 2020: Momentum flux measurements in the airflow over wind-generated surface waves. *J. Fluid Mech.*, **895**, A15, https://doi.org/10.1017/jfm.2020.276.

Zakharov, V. E., 1968: Stability of periodic waves of finite amplitude on the surface of a deep fluid. *J. Appl. Mech. Tech. Phys.*, **9**, 190–194, https://doi.org/10.1007/BF00913182.

Zemba, J., and C. A. Friehe, 1987: The marine atmospheric boundary layer jet in the Coastal Ocean Dynamics Experiment. *J. Geophys. Res.*, **92**, 1489–1496, https://doi.org/10.1029/JC092iC02p01489.

Zhang, J. A., P. G. Black, J. R. French, and W. M. Drennan, 2008: First direct measurements of enthalpy flux in the hurricane boundary layer: The CBLAST results. *Geophys. Res. Lett.*, **35**, L14813, https://doi.org/10.1029/2008GL034374.

Zhang, W.-Y., W.-X. Huang, and C.-X. Xu, 2019: Very large-scale motions in turbulent flows over streamwise traveling wavy boundaries. *Phys. Rev. Fluids*, **4**, 054601, https://doi.org/10.1103/PhysRevFluids.4.054601.

Zou, Z., J. Song, P. Li, J. Huang, J. A. Zhang, Z. Wan, and S. Li, 2019: Effects of swell waves on atmospheric boundary layer turbulence: A low wind field study. *J. Geophys. Res. Oceans*, **124**, 5671–5685, https://doi.org/10.1029/2019JC015153.